

12-1-2015

## High Pressure X-Ray Absorption Spectroscopy Studies of Heavy-Fermion Cerium and Uranium Compounds

Daniel Antonio

University of Nevada, Las Vegas, antonio@unlv.nevada.edu

Follow this and additional works at: <https://digitalscholarship.unlv.edu/thesesdissertations>

 Part of the [Physics Commons](#)

---

### Repository Citation

Antonio, Daniel, "High Pressure X-Ray Absorption Spectroscopy Studies of Heavy-Fermion Cerium and Uranium Compounds" (2015). *UNLV Theses, Dissertations, Professional Papers, and Capstones*. 2511. <https://digitalscholarship.unlv.edu/thesesdissertations/2511>

This Dissertation is protected by copyright and/or related rights. It has been brought to you by Digital Scholarship@UNLV with permission from the rights-holder(s). You are free to use this Dissertation in any way that is permitted by the copyright and related rights legislation that applies to your use. For other uses you need to obtain permission from the rights-holder(s) directly, unless additional rights are indicated by a Creative Commons license in the record and/or on the work itself.

This Dissertation has been accepted for inclusion in UNLV Theses, Dissertations, Professional Papers, and Capstones by an authorized administrator of Digital Scholarship@UNLV. For more information, please contact [digitalscholarship@unlv.edu](mailto:digitalscholarship@unlv.edu).

HIGH PRESSURE X-RAY ABSORPTION SPECTROSCOPY STUDIES OF HEAVY-  
FERMION CERIUM AND URANIUM COMPOUNDS

by

Daniel Antonio

Bachelor of Science - Physics  
University of Nevada, Las Vegas  
2004

Master of Science - Physics  
University of Nevada, Las Vegas  
2009

A dissertation submitted in partial fulfillment  
of the requirements for the

Doctor of Philosophy - Physics

Department of Physics and Astronomy  
College of Sciences  
The Graduate College

University of Nevada, Las Vegas  
December 2015

**Dissertation Approval**

The Graduate College  
The University of Nevada, Las Vegas

November 13, 2015

This dissertation prepared by

Daniel Antonio

entitled

High Pressure X-Ray Absorption Spectroscopy Studies of Heavy-Fermion Cerium and Uranium Compounds

is approved in partial fulfillment of the requirements for the degree of

Doctor of Philosophy – Physics  
Department of Physics and Astronomy

Andrew Cornelius, Ph.D.  
*Examination Committee Chair*

Kathryn Hausbeck Korgan, Ph.D.  
*Graduate College Interim Dean*

Michael Pravica, Ph.D.  
*Examination Committee Member*

Ravhi S. Kumar, Ph.D.  
*Examination Committee Member*

Thomas Hartmann, Ph.D.  
*Graduate College Faculty Representative*

## Abstract

Investigations into f- electron heavy-fermion materials have revealed a wide range of novel behavior. Hydrostatic pressure is a valuable "clean" non-thermal parameter that can be used to systematically study them by tuning their ground state properties. The rare earth compound  $\text{CeCu}_2\text{Ge}_2$  shows an unusual two-domed region of unconventional superconductivity under pressure, similar to its isostructural counterpart  $\text{CeCu}_2\text{Si}_2$ . While the lower pressure dome at about 10 GPa is caused by a magnetic quantum critical point (QCP), the higher one at about 16 GPa is less well understood. Previous structural measurements have indicated that it may be caused by critical valence fluctuations, so in this study the valence of  $\text{CeCu}_2\text{Ge}_2$  is directly measured using X-ray Absorption Near Edge Spectroscopy (XANES) under pressure in a diamond anvil cell up to 20 GPa. An expected valence discontinuity is not seen, but comparisons to  $\text{CeCu}_2\text{Si}_2$  show interesting similarities. Uranium's 5f electrons are intermediate between localized and delocalized. Studying the degree of localization is vital to completely understand the properties of actinides. Performing XANES and Partial Florescence Yield (PFY) measurements in a diamond anvil cell to tune the distance between uranium atoms, I have measured the energy shift in the white line of  $\text{UCu}_2\text{Si}_2$ ,  $\text{U}_3\text{Ni}_5\text{Al}_{19}$ , and  $\text{UCd}_{11}$  with pressure. A positive shift in energy indicated a delocalization of 5f electrons, a change in 5f configurations, or a combination of both.

## Table of Contents

Abstract .....	iii
Table of Contents .....	iv
List of Figures .....	v
Chapter 1: Introduction .....	1
Heavy Fermion Materials .....	1
Quantum Critical Points.....	2
Intermediate Localization of Electrons.....	4
CeCu <sub>2</sub> Ge <sub>2</sub> .....	7
CeCoSi.....	8
UCd <sub>11</sub> .....	9
U <sub>3</sub> Ni <sub>5</sub> Al <sub>19</sub> .....	10
UCu <sub>2</sub> Si <sub>2</sub> .....	11
X-ray Absorption Spectroscopy .....	11
EXAFS.....	13
XANES .....	13
Measuring XAS.....	16
XRD.....	19
Diamond Anvil Cells .....	21
Chapter 2: Experimental Procedure .....	26
Cerium Samples .....	26
Uranium Samples .....	28
Chapter 3: Results .....	33
Cerium Compounds.....	33
Uranium Compounds.....	36
Chapter 4: Conclusions .....	38
Appendix: Figures.....	39
Appendix: Tables .....	87
References .....	88
Curriculum Vitae .....	95

## List of Figures

Figure 1. Examples of Heavy-Fermion Materials with High Sommerfield coefficients. ....	39
Figure 2. Phase Diagram showing a QCP in a heavy fermion material.....	40
Figure 3. A modified periodic table showing trends in localization. ....	41
Figure 4. Plot relating energy shift of the $L_3$ edge to the Sommerfield coefficient.....	42
Figure 5. Crystal structure of $CeCu_2Ge_2$ . ....	43
Figure 6. Phase Diagram of $CeCu_2Ge_2$ . ....	44
Figure 7. The Superconducting region split .....	45
Figure 8. The two distinct superconducting phases in $CeCu_2Ge_2$ .....	46
Figure 9. Proposed isostructural volume collapse in $CeCu_2Ge_2$ .....	47
Figure 10. The crystal structure of $CeCoSi$ .....	48
Figure 11. Phase diagram for $CeCoSi$ .....	49
Figure 12. Crystal structure of $UCd_{11}$ . ....	50
Figure 13. The crystal structure of $U_3Ni_5Al_{19}$ .....	51
Figure 14. The crystal structure of $UCu_2Si_2$ .....	52
Figure 15. XAS Edges.....	53
Figure 16. General XAS profile.....	54
Figure 17. XAFS and XANES scattering pathways .....	55
Figure 18. The fluorescence energy level diagram of the uranium $L_3$ edge .....	56
Figure 19. Braggs Law. ....	57
Figure 20. High Pressure Powder Diffraction Geometry.....	58
Figure 21. An Example Raw Powder Diffraction Image .....	59
Figure 22. An Example Integrated XRD Pattern.....	60

Figure 23. A Cutaway diagram of a typical diamond anvil cell .....	61
Figure 24. The online ruby spectrometer at HPCAT sector 16-IDB .....	62
Figure 25. An example diagram of a ruby fluorescence detector .....	63
Figure 26. Almax-Easylab CuBe non-magnetic Pressure cell .....	64
Figure 27. The energy dependence of some absorption coefficients .....	65
Figure 28. Perforated diamond anvils. ....	66
Figure 29. A cutaway of a DAC with a gas membrane drive.....	66
Figure 30. A diagram of a gas membrane pressure controller.....	67
Figure 31. A Paderborn-panoramic style DAC with beryllium gasket.....	67
Figure 32. A Princeton Mao-type symmetric cell.....	68
Figure 33. The radial scattering geometry used in PFY acquisition. ....	68
Figure 34. A four-posts wide-opening DAC. ....	69
Figure 35. The evolution of the CeCu <sub>2</sub> Ge <sub>2</sub> L <sub>3</sub> edge with Pressure at 10 K.....	70
Figure 36. The evolution of the CeCoSi L <sub>3</sub> edge with pressure .....	71
Figure 37. Example of the fit to the intensity of the white line for CeCu <sub>2</sub> Ge <sub>2</sub> .....	72
Figure 38. The change in Cerium Valence vs. Pressure of CeCu <sub>2</sub> Ge <sub>2</sub> .....	73
Figure 39. Ce valence from XANES data as a function of pressure for CeCoSi .....	74
Figure 40. Comparison of Ce valence from CeCu <sub>2</sub> Ge <sub>2</sub> with CeCu <sub>2</sub> Si <sub>2</sub> .....	75
Figure 41. Conversion to f electron occupancy vs. unit cell volume.....	76
Figure 42. Single crystal XRD data of CeCoSi at 6 GPa.....	77
Figure 43. The a, b, and c lattice parameters in CeCoSi as a function of pressure. ....	78
Figure 44. Unit cell volume as a function of pressure of CeCoSi .....	78
Figure 45. Equation of state for U <sub>3</sub> Ni <sub>5</sub> Al <sub>19</sub> .....	79
Figure 46. Equation of state for UCd <sub>11</sub> .....	80
Figure 47. Evolution of the white line under pressure for U <sub>3</sub> Ni <sub>5</sub> Al <sub>19</sub> . ....	81

Figure 48. The shift in the white line of $U_3Ni_5Al_{19}$ .....	82
Figure 49. Evolution of the white line under pressure for $UCu_2Si_2$ .....	83
Figure 50. The shift in the white line of $UCu_2Si_2$ .....	84
Figure 51. Evolution of the white line under pressure for $UCd_{11}$ .....	85
Figure 52. Shift in White line peak from ambient pressure for $UCd_{11}$ .....	86



## Chapter 1: Introduction

### *Heavy Fermion Materials*

Strongly correlated electron materials are a general class of compounds that often have unusual electronic and magnetic properties. When the electrons in a material are weakly correlated and can be modeled as non-interacting entities, such as a free electron gas in metallic solids [1], their behavior can be completely solved analytically. Strongly correlated materials, however, are defined by the strong interactions between their electrons that cannot be ignored when describing their behavior [2]. The wide range of materials that fall under this class include high  $T_c$  superconducting cuprates, such as bismuth strontium calcium copper oxide [3], and Mott insulators, which should conduct electricity under conventional band theories but do not [4]. Different methods are required in order to explain their behavior, such as the Landau Fermi Liquid model, where the ensemble of real particles is substituted by quasiparticles, which are long-lived excitations that weakly interact with each other via some effective interaction potential [5]. In the Fermi Liquid model, the electrons behave in the same manner as free electrons with the exception that the electron mass is renormalized.

Heavy fermion compounds are a specific type of strongly correlated material that contains rare earth or actinide elements where the renormalized effective mass is very large (sometimes in excess of 1000 times the free electron mass). The conduction electrons indirectly interact with each other by scattering off of the large magnetic moments of the unpaired 4f or 5f electrons. This is called the Kondo effect, where at low enough temperatures (below the so called Kondo temperature  $T_K$ ) a magnetic spin and a correlated conduction electron cloud can bind very strongly to form a non-magnetic state. This interaction forms a Fermi liquid with

quasiparticles that have an effective mass much greater than electrons, which gives these materials their name [6]. The strength of this interaction between the f electrons and the conduction electrons ( $T_K$ ) can be found by many measurements. One such measurement comes from a characteristic large linear term of the heat capacity of the material at low temperature, called the Sommerfeld coefficient ( $\gamma$ ), where  $T_K \propto 1/\gamma$ . In fact, this value is an incredibly important factor related to all properties of a heavy-fermion material. Some examples of low temperature heat capacity of heavy-fermion materials showing a high Sommerfeld coefficient compared to a conventional material, copper, are shown in Figure 1 [7, 8, 9, 10]. The Sommerfeld coefficient can also be used as an effective measurement of the localization of the f electrons [11]. It is proportional to the effective carrier mass, which means it is proportional to the density of states at the Fermi level [12]. Since a flat, atomic-like band corresponds to a high  $\gamma$ , this could be considered an indicator of more localized character due to a higher f-orbital occupancy [13].

### *Quantum Critical Points*

The strong localized moments due to the unpaired f electrons in metals give rise to a mechanism that competes with the Kondo effect, called the Ruderman-Kittel-Kasuya-Yosida (RKKY) interaction [14, 15, 16]. The inner electron spins are coupled to conduction electron spins by the exchange interaction, and those conduction electron spins are coupled to other unpaired f electron spins in the lattice, thereby indirectly correlating the spins in the lattice. At low enough temperature, this gives rise to a magnetically ordered state that competes with the non-magnetic Kondo state. Tuning the relative magnitudes of these opposing effects by chemical substitution, applying magnetic field, or increasing pressure can cause a quantum critical point (QCP) to be formed, such as in  $\text{CeCu}_2\text{Si}_2$ . [17].

A quantum critical point occurs when a continuous second order phase transition that occurs at finite temperature is driven to zero Kelvin [18,19]. Though it is possible for such a state to exist under normal conditions at low temperature, usually a tuning parameter such as pressure, magnetic field, or chemical substitution is used to drive the phase transition to zero Kelvin. A generalized phase diagram is shown in Figure 2 [20]. The collective quantum mechanical fluctuations control the physics of the material in the vicinity of the QCP. This leads to unusual ground states with non-Fermi liquid (NFL) behavior that can have unusual magnetic structures and other characteristic effects such as a power law temperature dependence of the specific heat. In fact, one signature of NFL behavior is a deviation from the Wiedemann-Franz law, which says that the ratio of a metal's thermal conductivity to its electrical conductivity is linearly dependent on temperature, as these values are determined by the quasi-particles in a Fermi liquid [Amusia pg 251]. One extensively studied effect is the emergence of unconventional superconductivity near QCPs.

Superconductivity in heavy-fermion systems has been the subject of intense study since the discovery of the first one,  $\text{CeCu}_2\text{Si}_2$ , in 1979 [21]. Other rare earth and actinide heavy fermion superconducting compounds have been discovered since. They do not behave like conventional superconductors, in which Cooper pairs (the attraction of a pair of electrons into a single boson quasiparticle) are mediated by phonon interactions and long range magnetic order is generally not allowed. The quantum fluctuations near QCPs may allow quantum-critical spin density waves to form which mediate formation of quasiparticles [17].

### *Intermediate Localization of Electrons*

In general, the 4f electron wave functions in lanthanides are held close to the atom and do not participate in bonding, giving rise to large well defined local moments. In contrast, the d electrons in transition metals are delocalized and have wave functions with a large spacial extent that overlap. This leads to the various orbitals having their density of states as a function of energy occurring together. This lets them interact strongly with ligand orbitals and the conduction band. The 5f electrons in the light actinides, however, tend to extend farther than the 4f electrons in lanthanides, but not as far as the d electrons in transition metals. This can lead to behavior that is intermediate between the localized and delocalized, which cannot be explained entirely by the local moment behavior (governed by the Kondo effect and RKKY interactions) or by the itinerate magnetism seen in 3d, 4d, and 5d transition metals. A few of the lanthanide ions also share this phenomenon, as shown in Figure 3. Plutonium remains the most mysterious of the actinides, which is at least partly due to its presence directly on this transition from local to itinerant 5f electrons. The result of this is a very complicated phase diagram (Plutonium has 6 allotropes at ambient pressure, the most of any element), as well as an extreme sensitivity to chemical impurities leading to inconsistent studies with wildly different structural phases under the same conditions, and physical properties and magnetic states that do not fit to known theories.

Uranium is much more studied, due to its importance in energy production and greater availability. Its physical properties are of great interest by itself, but also as an analogue to plutonium. Like plutonium, uranium has several common oxidation states. It can commonly be found in 3+, 4+, and 5+ states concurrently, which can lead to complex magnetic behavior in a mixed valence compound, where some electrons are itinerant and others remain localized.

Cerium, however, has only two common oxidation states: 3+ that is definitely magnetic, and 4+

which is definitely not due to a complete absence of unpaired f electrons. Most lanthanides are commonly only found in the 3+ state, but cerium, ytterbium, and europium have 2 common states due to the stability of the empty, half-filled, and completely filled valence shells, respectively. This leads heavy fermion cerium and ytterbium compounds to having similar processes and effects to those seen in actinides, but in a simpler to study system. It is also interesting to study Ce and Yb compounds at pressure as Ce is driven away from a magnetic state while Yb is driven toward a magnetic state as pressure increases.

Itinerant behavior of the 5f electrons is not usually expected in uranium compounds unless the inter-atomic spacing between the uranium atoms is below the Hill limit, which is about 3.4 to 3.6 Å [39]. This is usually independent of whatever other atoms are in the compound. Below this spacing, the wave functions of the f electrons begin to overlap, the uranium atoms are usually nonmagnetic, and conventional superconductivity is possible. Above this, the uranium atoms tend to be localized and magnetic. Heavy fermion uranium compounds are an exception to this, as they can condense into a superconducting state around a QCP even if there is a large interatomic spacing, leading one to conclude that the superconductivity is unconventional in nature.

Elements in a compound that exhibit different valence states will have a white line that shows multiple peaks when measuring XANES (explained later in this dissertation), with each peak corresponding to one of the multiple edge energies due to the different valence states present. The relative intensities of those peaks are proportional to the occupancy of those valence states, so a ratio of the peak intensities can give the fractional valence of the absorbing atom. For mixed valence cerium compounds at the  $L_3$  edge this is straightforward. There are only two valence states and the white lines corresponding to the valence states are well separated

(~ 10 eV), while the core-hole lifetime broadening of the transition is only 3.48 eV [61], and instrumental broadening is typically on the order of 1 eV.

The uranium  $L_3$  edge is different, as there are 3 possible states which are not as well separated (~5 eV between each), and the core hole broadening increases with the atomic number  $Z$ , going to 7.43 eV for uranium. This makes the individual peaks wash out and not be distinguishable. However, a fit of a single peak to the white line of uranium can give a general idea of the oxidation state. As the oxidation state increases the peak will shift to higher energies, meaning that the electron occupancy decreases and therefore the shielding of the nucleus decreases. Decreasing electron occupancy at the atom's site implies the electrons are becoming more itinerant. This means that the shift in edge energy and the Sommerfeld coefficient should show a correlation, which has been investigated in Booth, *et. al.* [11]. As seen in Figure 4, the energy shift ( $\Delta E$ ) in the white line compared to the alpha uranium ( $\alpha$ -U) white line was plotted vs. the Sommerfeld coefficient ( $\gamma$ ) of 17 heavy fermion intermetallic uranium compounds [11]. The samples, which were all measured at ambient pressure and low temperature, show a mostly linear dependence between the parameters, with  $\alpha$ -U having the lowest  $\gamma = 9.13 \text{ mJ/ mol-K}^2$ , and  $\text{UCd}_{11}$  having by far the highest  $\gamma = 840 \text{ mJ/ mol-K}^2$  at a  $\Delta E = 6.6 \text{ eV}$  [11]. Using the white line shift between uranium oxides with well-known oxidation states, a shift of about 4 eV corresponds to a change in occupancy of about 1 electron. Varying screening effects from conduction electrons can cause deviations in this general trend, such as with  $\text{UPd}_3$  [22, 23], but they remain fairly constant between the metals.

## $CeCu_2Ge_2$

$CeCu_2Ge_2$  has the same  $ThCr_2Si_2$  tetragonal crystal structure, seen in Figure 5, as the first heavy fermion superconductor discovered,  $CeCu_2Si_2$  and the entire series  $Ce(Cu_2(Si_{1-x}Ge_x)_2)$  can be synthesized as Ge substitution expands the tetragonal lattice. It has a complicated pressure vs. temperature phase diagram, shown in Figure 6 [24]. For ambient pressure at low temperature, the RKKY interaction dominates, leading to an antiferromagnetic magnetically ordered state. As pressure is increased, the Kondo coupling begins to dominate, leading to a heavy fermion state. At the point where this transition is driven to zero Kelvin, a quantum critical point (QCP) is formed around 10 GPa and a superconducting dome appears. It is an unconventional superconductor, as the cerium valence is nearly 3+ and therefore strong localized magnetic moments are present. Strangely, the superconducting dome is very asymmetrical and has its highest  $T_c$  at 16 GPa. This unusually shaped superconducting dome is also seen in  $CeCu_2Si_2$ , which has a similar phase diagram, where one needs to only shift down the superconducting dome to have a maximum  $T_c$  at about 5 GPa [25]. A study of  $CeCu_2(Si_{0.9}Ge_{0.1})_2$  revealed that by using chemical substitution to introduce disorder in  $CeCu_2Si_2$  and effectively apply negative pressure (as mentioned Ge is bigger than Si), the superconducting region could be split into two separate domes, with non-Fermi liquid behavior between them, as shown in Figure 7 [26]. This gave strong evidence that a second QCP was present in both materials, giving rise to two distinct, overlapping superconducting states, as in Figure 8 [27].

Due to a coincidence of peaks of the residual resistivity and the superconducting transition temperature, it was proposed that this could be due to a rapid valence change in the Ce ion [28, 29]. In an XRD measurement of  $CeCu_2Ge_2$  at cryogenic temperatures Onodera *et al.* claimed to have seen an isostructural volume collapse in the crystal structure at about 16 GPa,

aligning with the maximum superconducting  $T_c$ , as seen in Figure 9 [30]. This would correspond to a sudden valence transition in the mixed valence state. The localized magnetic  $Ce^{3+}$  ion has a larger ionic radius than the smaller  $Ce^{4+}$  ion that has had its f electron promoted to the conduction band, so it is natural for it to transition to a more  $Ce^{4+}$  like character as pressure is increased. However, more recent XRD studies of  $CeCu_2Ge_2$  and  $CeCu_2Si_2$  have not revealed any similar volume collapse [32]. Vegard's law states that the lattice parameter of a solid solution of two materials with the same crystal structure is equal to a simple mixture of the two constituents [33], given by:

$$a_{A_{(1-x)}B_x} = (1 - x)a_A + xa_B \quad \text{Equation 1.}$$

where  $a_{A_{(1-x)}B_x}$  is the lattice parameter of the solution,  $a_A$  and  $a_B$  are the lattice parameters of the pure forms, and  $x$  is the molar fraction of  $B$  in the solution. Therefore, the volume of a chemical mixture should be linearly between the two volumes of the pure unit cells. Using average values for the ionic radii of cerium in oxides, the volume difference between purely  $Ce^{4+}$  and purely  $Ce^{3+}$  of the same  $CeCu_2Ge_2$  structure would be ~20%. In order to account for the 2% volume collapse reported in Onodera *et al.* [Onodaera], a 0.1 valence discontinuity should be seen. A valence transition of that magnitude would easily be detected in a XANES measurement of  $CeCu_2Ge_2$  under pressure.

### *CeCoSi*

Among Ce based HF compounds,  $CeCoSi$  is particularly interesting since it has been shown to display complicated pressure dependent behavior typical of Ce HF systems[34]. Like other  $RCoSi$  materials, at ambient pressure  $CeCoSi$  crystallizes in a layered tetragonal structure (P4/nmm) with  $a = 0.4046$  nm,  $c = 0.6969$  nm) [35] shown in Figure 10. Co is tetrahedrally



coordinated with Si atoms having a Co-Si distance of 0.238 nm. These tetrahedra share corners and edges and arrange into a 2 dimensional array of pyramidal cavities. Above the apices of these pyramidal cavities Ce resides with the shortest Ce-Si distance of 0.304 nm. CeCoSi is antiferromagnetically ordered at ambient pressure with  $T_N \approx 9$  K [37]. High pressure measurements show a complex magnetic behavior with multiple phases with magnetism terminating in a quantum critical point (QCP) near 2 GPa [34]. It has a complex phase diagram containing signatures of a structural transition, valence transition, charge density wave, and superconductivity, shown in Figure 11 [36]. At pressures above 3 GPa a strong hysteretic phase transition was observed where there is a strong decrease in resistivity below  $T_v$  shown in Fig. RR. This behavior is similar to that observed in other systems where a valence transition is observed. Namely, valence transitions display a hysteretic (first-order) transition that is strongly pressure dependent. By 4 GPa, the transition moves above room temperature. Because of this complex behavior, we have studied the electronic and structural properties of CeCoSi above the QCP at pressures to 10 GPa. The interplay between the various structural and electronic properties points towards the formation of superconductivity far away from magnetic order in a charge density state.

### *UCd<sub>11</sub>*

UCd<sub>11</sub> is an interesting binary heavy fermion uranium intermetallic compound that has a very large nearest U-U spacing and, therefore, minimal 5f-5f orbital interactions. It crystallizes in the cubic BaHg<sub>11</sub>-type structure with a lattice constant of 9.29 Å, shown in Figure 12, and has a nearest U-U neighbor distance of 6.56 Å [38]. This distance of 6.56 Å is very large compared to the Hill limit [39] and overlapping of neighboring 5f wavefunctions is expected to be minimal. In spite of the absence of direct 5f-5f interactions, it forms a complex magnetic ground state [40]

and orders antiferromagnetically at  $T_N \approx 5$  K [38]. The magnetic susceptibility above 80 K follows a Curie-Weiss law with an effective magnetic moment of  $\mu_{\text{eff}} = 3.45 \mu_B/\text{U}$  whereas below 80 K it deviates from the Curie-Weiss law and finally attains a constant value below 5 K [38]. Low-temperature pressure and magnetic field dependent resistivity, specific heat and magnetization data revealed additional transitions below 5 K to a complex magnetically ordered ground state [40, 41, 42, 7]. Its electronic specific heat Sommerfeld coefficient,  $\gamma = 803 \text{ mJ/mol-K}^2$ , in the paramagnetic region, is the highest for any ordered uranium heavy fermion system [43]. Despite being very localized compared to other heavy fermion uranium intermetallics, resonant X-ray emission spectroscopy (RXES) measurements show that its 5 f orbital has an occupancy of  $2.7 \pm 0.2$ , and so is not entirely in the  $\text{U}^{3+}$  configuration [11].

### *U<sub>3</sub>Ni<sub>5</sub>Al<sub>19</sub>*

The heavy fermion material  $\text{U}_3\text{Ni}_5\text{Al}_{19}$  crystallizes in the orthorhombic  $\text{Ge}_3\text{Ni}_5\text{Al}_{19}$  structure [44] (space group Cmc<sub>2</sub>m) with two inequivalent U sites (one U atom in 4c and two U atoms in 8f), shown in Figure 13. It has a large unit cell at ambient pressure with lattice parameters  $a = 4.0850(2) \text{ \AA}$ ,  $b = 15.9305(8) \text{ \AA}$ , and  $c = 26.959(1) \text{ \AA}$  [45]. Its nearest neighbor U-U distance is  $4.085 \text{ \AA}$ , which is above the Hill limit.  $\text{U}_3\text{Ni}_5\text{Al}_{19}$  orders antiferromagnetically at  $T_N = 23$  K, as determined from a prominent feature in the magnetic susceptibility involving one of the two distinct U sites, while the other site showed no sign of magnetic order down to 50 mK. It has a Sommerfeld coefficient of  $\gamma = 80 \text{ mJ/mol-U K}^2$ , but shows evidence of critical spin fluctuations in the magnetic contribution to the specific heat and a power law dependence of the resistivity at zero pressure, indicating that there is a QCP near zero pressure [45]. A Fermi liquid ground state returns briefly as pressure is applied between about 4 and 5 GPa, but the power law dependence returns, indicating that a second antiferromagnetic QCP occurs near 6 GPa. It is

unclear if either one or a combination of both of the inequivalent uranium sites is responsible for the antiferromagnetic order and the non-Fermi liquid behavior.

### *UCu<sub>2</sub>Si<sub>2</sub>*

The heavy fermion material UCu<sub>2</sub>Si<sub>2</sub> also crystalizes in the body centered tetragonal ThCr<sub>2</sub>Si<sub>2</sub>-type structure (space group *I4/mmm*)[46], shown in Figure 14. It has lattice parameters  $a = 3.985(1) \text{ \AA}$  and  $c = 9.945(2) \text{ \AA}$ , with a nearest neighbor U-U spacing of  $3.985 \text{ \AA}$ , which is above the Hill limit, and has  $\gamma = 20 \text{ mJ/mol U-K}^2$  [47]. It is a Kondo-like ferromagnet below about 105 K, but there has been some controversy over whether there is a transition to antiferromagnetic order at 50 K [48, 49]. Strong magnetic fluctuations appear to coexist with the long range magnetic order, indicating that there may be a superconducting transition at high pressure. High pressure magnetic measurements were taken up to 2 GPa, but it was concluded that much higher pressure would be needed to reach a QCP [50].

### *X-ray Absorption Spectroscopy*

X-ray Absorption Spectroscopy (XAS) has become an enormously useful diagnostic tool. The fine structure around the absorption edges of metallic atoms was first noticed on photographic plates in 1913, fairly soon after the discovery of X-rays, and the basic theory behind it was explained about a decade later. However, it was not until generated X-ray flux was increased with the development of high intensity synchrotron radiation sources with storage rings in the 1970's that could replace discharge tubes and fast high resolution detectors that modern XAS took off [55]. It allows the local electronic and geometric structure around a specific type of atom in a material to be probed, as opposed to another common technique, X-ray diffraction (XRD), which obtains average values for a structure over a long range in a bulk material. These

different techniques can often be used to complement each other in order to gain a much more complete understanding of the materials being studied.

The process of XAS involves varying the energy of incoming monochromatic X-rays across an absorption edge of a desired atom, which is the energy required to excite a core electron to a higher unoccupied bound or continuum state leaving behind a core hole, and measuring the absorption profile of the material in one of several ways. Every atom has multiple absorption edges at different characteristic energies, corresponding to different core electrons that can be excited. The different absorption edges are defined by the starting states of the core electrons being excited. The principal quantum numbers  $n = 1, 2,$  and  $3$  correspond to the K, L, and M edges, respectively. They are further divided by subscripts corresponding to the azimuthal quantum number and spin orbit coupling, as shown in Figure 15 [56]. The K and  $L_1$  edges involve transitions from s to p states, while the  $L_2$  and  $L_3$  edges go from p to final states that are a mixture of d and s character.

When the individual incoming photons reach and then exceed the energy required for that core electron to absorb one and become excited, a sudden step-like increase in the absorption is seen. This resulting sudden increase in the absorption spectrum and the fine structure around it can give a large amount of information, as different processes dominate the fine structure depending on the energy range around the absorption edge being studied as shown in Figure 16 [manchester]. The part of the spectrum roughly 50 eV above and below the absorption edge is referred to as X-ray absorption near edge structure (XANES), which corresponds to the point where the wavelength of the excited electron is about equal or less than the distance between the absorbing atom and its nearest neighbors [54]. The range from this limit up to about 1000 eV higher is referred to as extended X-ray absorption fine structure (EXAFS).

## *EXAFS*

EXAFS was first explained as weak single scattering of the excited electron off of neighboring atoms to the absorbing atom [58] [59]. The core electron is ejected and the left over energy above that required exciting it to an unbound state is transferred to that photoelectron. In the EXAFS region of the absorption spectrum the wavelength of this electron is larger than the interatomic distance between the absorbing atom and its nearest neighbors, resulting in a lower likelihood of this photoelectron interacting with those nearest neighboring atoms. The spectrum's features are due to the wave nature of the excited photoelectron, with the fine structure of periodic peaks and valleys occurring as the backscattered and outgoing waves come in and out of phase. A Fourier transform can be used to deconvolute the decaying sinusoidal signals and recover the frequency and intensity of the patterns that correspond to the different individual neighboring atoms [60]. This allows for the determination of interatomic distances as well as types and numbers of atoms at these distances surrounding the absorbing atom. Because the effect is entirely dependent on backscattering from the absorbing atom's immediate surroundings, EXAFS does not occur or have any meaning for isolated atoms. This also means that the technique can be applied to amorphous and molecular materials just as easily as regularly repeating crystalline solids, as only the local structure around any single absorbing atom contribute to the effect.

## *XANES*

XANES has difficulties compared to EXAFS, as the scattering in this energy range is stronger and more complex than in EXAFS. Generally higher resolution spectra are also

required, with ~6 eV bandwidth being sufficient for EXAFS, but an order of magnitude higher resolution is preferable for XANES [51].

In the region about 50 eV below the edge step, pre-edge features can often be seen. These usually correspond to the core electrons transitioning to bound states, according to the dipole selection rules:

$$\Delta l = \pm 1, \Delta j = \pm 1, \Delta s = 0 \quad \text{Equation 2.}$$

Weaker forbidden transitions are often seen too, however, due to orbital mixing and quadrupolar coupling.

In the energy range up to about 50 eV above the edge, the wavelength of the photoelectron is smaller than the nearest neighboring atomic distances, leading to strong scattering off of these neighboring atoms. Multiple scattering effects due to higher order atomic correlations are significant, so the single scattering effects that dominate in EXAFS cannot be used to explain the fine structure. A general example of the difference is shown in Figure 17 [51]. Every allowable scattering path off of multiple atoms adds to the interference pattern. Not only the radial distances, but also local arrangements and bond angles become significant parameters. This can cause similar structures around an absorbing atom to have superficial similarities in the XANES fine structure that can be qualitatively compared.

The core state being excited is essentially the same as in an isolated atom, though its environment affects the higher energy states to which the electron is being excited. These possibly include unoccupied parts of *s*, *p* and *d* bands and low-lying continuum states. The multiple scattering at lower energies in the XANES region also transitions smoothly to single scattering in the EXAFS region at higher incoming X-ray energies. A theoretical analysis would

require solving the Schrödinger equation for a range of energies, where at lower energy the interaction of the electrons with these low lying energy states in the atoms is strong, to the higher energy limit at EXAFS, where the interaction with the atoms is weak [52]. Until the development of newer and more powerful computers and software relatively recently these types of calculations were not practical, though they still remain difficult for more complicated structures. This leaves qualitative comparison of spectra to be the most useful analysis in some cases, as similar local structures can lead to distinct features.

In the near edge region within about 8 eV is also where a quasiatomic effect called a “white line” occurs in transition metals and rare earth elements. These are so named due to this large absorption peak being observed as an unexposed band on the photographic films first used to detect them [53]. The existence of a sharp intense absorption band indicates that the final state is highly confined by the potential it sees [63]. In this work, we will define the white line position by the local maximum that is observed in absorption versus energy plots, as seen in Figure 16. The more localized *d* final states are less diffuse than the final *p* states, which can lead to sharper peaks for the  $L_2$  and  $L_3$  edges, though all *K* and *L* edges can show a well-defined white line. At the  $L_3$  edge, this is due to the well-defined  $2p$  to  $nd$  transitions. The shape and intensity of the white line can also depend on the amount of hybridization between the *p* and *d* bands. In this region the photoelectron is scattered elastically by the valence electrons and its final states are near the Fermi level. The fully screened core hole makes the transition atomic like, with the broadening of the peak mainly due to the core hole lifetime. In insulators, the core hole is only partially screened which causes a photoelectron- core hole Coulomb attraction, making the absorption threshold much less well defined and removing the distinct white line feature. Changes in the charge distribution around a given atom due to its local environment will

alter the core-level binding energies, producing an edge shift in the absorption edge. This makes the energy shift of the white line particularly useful in measuring the oxidation state of the absorbing atom.

### *Measuring XAS*

Two different methods were used to measure the X-ray absorption spectra, each offering advantages and disadvantages over the other.

#### **Transmission mode**

The more commonly used technique is done in transmission geometry. Two X-ray detectors are put in the path of the X-ray beam, one before the sample and one after. Typical detectors are either diodes or ion chambers filled with air or some inert gas, depending on the energy range of the edge being probed. The absorption profile is then calculated as a ratio of the intensity of the initial X-ray beam ( $I_0$ ) to the outgoing beam ( $I'$ ), given by:

$$A = \log \frac{I_0}{I'} \quad \text{Equation 3.}$$

and is measured as a function of the energy of the incoming X-ray beam.

Though the calculation is straightforward, care must be given to make sure that the sample is well prepared in order to extract good data. The sample must be of uniform thickness and density over the entire area of the X-ray beam, or else the signal will be flattened due to an averaging of the different absorption lengths over the whole sample. The sample does not need to be pure, however, as long as any material mixed with it is sufficiently transparent to the X-rays and it does not contain any of the same absorbing element being investigated. This can be



used to alter the density of the sample in order to bring it to a proper absorption length for a particular experimental arrangement. The absorption profile is essentially a measurement of the linear absorption coefficient ( $\mu$ ) according to the Beer-Lambert law [62]:

$$I' = I_o e^{-\left[\frac{\mu}{\rho}\right]\rho_t x} \quad \text{Equation 4.}$$

with:

$$\frac{\mu}{\rho} = \sum_i w_i \left(\frac{\mu}{\rho}\right)_i \quad \text{Equation 5.}$$

where  $\frac{\mu}{\rho}$  is the total mass absorption coefficient of the sample at the incoming X-ray energy,  $\rho_t$  is the total density,  $x$  is the total sample thickness, and  $w_i$  and  $\left(\frac{\mu}{\rho}\right)_i$  are the mass fraction and X-ray mass absorption coefficients of the individual elements making up the sample, respectively. The characteristic absorption length is then defined as the sample thickness that reduces the incoming intensity of the X-ray beam by a factor of  $\frac{1}{e}$ . In a statistically ideal case, a sample with total thickness of 2.6 absorption lengths gives a good signal to noise ratio [64]. However, a sample will also have a change in absorbance going from below to above the absorption edge of the measured element as the energy is scanned, called the edge step:

$$\Delta\mu x = \mu(E_i)x - \mu(E_o)x \quad \text{Equation 6.}$$

where  $E_i$  and  $E_o$  are the energies just below and above the absorption edge. Ideally, this is also about  $\frac{1}{e}$ , where values as low as 0.1 and as high 1.5 can give acceptable signal to noise ratios.

This leads to competition in the ideal sample thickness between the total absorbance of the sample and the edge step of the sample, and this means that individual sample geometries

involve tradeoffs. Samples with dilute absorbing elements inside heavily absorbing mediums can be particularly challenging.

### **Florescence Mode**

It can be useful to instead look at the florescence profile of the edge instead of the absorption profile. Partial florescence yield (PFY), which is sometimes called XANES in florescence mode, indirectly probes the same dynamics, but can offer some advantages over the transmission method [65]. When the X-rays excite a core electron and leave behind a core-hole, another electron falls to the lower empty state and emits a photon, as in this example for the Uranium  $L_3$  edge in Figure 18 [11]. A high-resolution spectrometer is situated 90 degrees to the incoming X-ray beam and tuned to the emission wavelength of that falling electron, separating that particular signal from the total florescence of the sample. This eliminates the need for the complicated sample geometry of the transmission mode measurements, as a completely uniform and flat sample is not needed. This method does however require a much more complex experimental set-up, needing a sensitive proportional X-ray detector and curved silicon mirrors to focus the floresced X-rays into it. A much higher flux 3rd generation insertion device beamline is also needed in order to carry out the experiment in a reasonable time with good statistics, giving sample signals on the order of hundreds of counts per second, as opposed to the hundreds of thousands of counts per second one would expect from the simpler ion chamber detectors of a transmission mode measurement. The need for longer times required and more advanced, and therefore more over-subscribed, beamlines make getting synchrotron time for florescence measurements more difficult. Ideally this emitted signal intensity from the florescence would be directly proportional to the absorption profile of the sample, but self-

absorption effects can lead to a non-smoothly varying energy correction factor. This can be avoided by using a sufficiently thin sample or dilute sample, rendering the correction negligible.

### *XRD*

Powder X-ray diffraction is a well-established and commonly used technique at synchrotrons in high-pressure cells. The high intensity X-rays allow for high quality diffraction patterns to be taken in seconds, and the greater penetrating power of higher X-ray energies (>10 keV) than copper or molybdenum anode sources allow for measurements to be made through diamond anvil cells. When the monochromatic beam hits the sample, diffraction occurs. If the angle of the X-rays to the crystal lattice plane meets the Bragg condition for constructive interference:

$$2d \sin \theta = n\lambda \qquad \text{Equation 7.}$$

Where  $d$  is the spacing between lattice planes,  $\theta$  is the scattering angle,  $n$  is a positive whole number, and  $\lambda$  is the X-ray wavelength, as shown in Figure 19. Typical values for  $\lambda$  are 10s of keV at a synchrotron. If the powder sample has uniformly small grains compared to the beam area, then all possible orientations are represented at the same time. This leads to cones of diffracted beams emanating from the sample corresponding to all possible lattice plane spacings as shown in Figure 20. They then hit an intensity sensitive area detector directly behind the sample opposite the incoming beam, producing a ring pattern. A raw sample image of  $\text{U}_3\text{Ni}_5\text{Al}_{19}$  taken at a pressure of 5 GPa in a diamond anvil cell is shown in Figure 21. Large spots outside the rings are due to diffraction off of large single crystals of the sample or the diamond anvil, which are removed during analysis. A known sample, usually cerium dioxide, is used to determine the exact distance and angle of the area detector in relation to the sample, which is

then used to integrate the radial intensities of the ring pattern into a 2D intensity vs  $2\theta$  plot using Fit2D [68, 69]. The integrated sample pattern of the previous  $U_3Ni_5Al_{19}$  image is given in Figure 22. These peaks can be matched and refined to one of the 230 known types of crystal symmetries, fairly easily obtaining the unit cell lattice parameters if the crystal symmetry is already known. Single crystal diffraction is better suited for determining an unknown structure, but powder diffraction is very useful for obtaining the equation of state of a material, which can be used to correlate interatomic spacings and possible structural changes in a material to changes in other properties.

Particularly useful to high-pressure physics is the change in volume vs. pressure of a material referred to as the equation of state (EOS). As the atoms in a material are forced closer together, its bulk structural and electronic properties can be radically changed. A simple visual inspection of an EOS curve can often reveal indications of this, as discontinuities in the smooth curve or sudden volume collapses are signs of structural or electronic transitions. In general, if there are no such discontinuities then the structure of the material remains the same as it is compressed. It will in general become less compressible as pressure is increased, which can be quantified by fitting the data to either the Birch–Murnaghan isothermal equation of state [70] or Rose–Vinet equation of state [71]. The 4<sup>th</sup> order Birch–Murnaghan equation is:

$$P(V) = \frac{3B_o}{2} \left[ \left( \frac{V_o}{V} \right)^{\frac{7}{3}} - \left( \frac{V_o}{V} \right)^{\frac{5}{3}} \right] \left\{ 1 + \frac{3}{4} (B'_o - 4) \left[ \left( \frac{V_o}{V} \right)^{\frac{2}{3}} - 1 \right] \right\} \quad \text{Equation 8.}$$

where  $V_o$  is the volume at zero pressure, the bulk modulus  $B_o$  is:

$$B_o = -V \left( \frac{\partial P}{\partial V} \right)_{P=0} \quad \text{Equation 9.}$$

and the derivative of the bulk modulus  $B_o'$  is:

$$B'_o = \left(\frac{\partial B}{\partial V}\right)_{P=0} \quad \text{Equation 10.}$$

The Rose–Vinet equation is a more universal modification of the Birch–Murnaghan equation that usually gives similar values for the bulk modulus:

$$P(V) = 3B_o \left(\frac{1-\eta}{\eta^2}\right) e^{\frac{3}{2}(B'_o-1)(1-\eta)} \quad \text{Equation 11.}$$

where:

$$\eta = \sqrt[3]{\frac{V}{V_o}} \quad \text{Equation 12.}$$

### *Diamond Anvil Cells*

Diamond anvil cells (DACs) are useful and versatile tools for exploring materials under extremely high pressures. Diamonds are the only readily available material that has the extraordinary compression strength necessary to attain these pressures. Maximum pressures achieved have reached several million atmospheres (hundreds of GPa as 1 GPa = 10 kbar= 10,000 atm) in carefully controlled instances using specialized anvils [72], but standard diamonds can be used to reliably and repeatedly reach pressures above 60 GPa. Diamonds also conveniently have many other useful properties that make them ideal. They have high transparency for making optical spectroscopic measurements and direct observation of the sample *in situ*. They are electrically insulating, which can be useful when making electronic transport measurements. Despite being a good electrical insulator, they also have a very high thermal conductivity, which can be useful for controlling and measuring temperatures in high temperature and thermal transport measurements. In general, DACs are also small enough to be easily transported and

put in small sample spaces (overall size less than an inch), such as cryostats, and can hold steady pressures for long periods of time. There are several noticeable drawbacks, though. Most notable is the limit of small sample size, with only a maximum of a few hundred microns at 10s of GPa, and only a few microns at 100s of GPa. Also, the limiting angular openings and allowable energies that can pass through the diamonds make some types of experiments unfeasible.

The basic parts of a DAC are show in Figure 23 [73]. Two opposed gem cut flawless diamonds are arranged in an apparatus with their culets (flat pressure transmitting surface) facing each other. Typical culet diameters range from about 250 microns to a millimeter. Larger culets offer more stability, at the cost of a lower maximum attainable pressure, working from the principle that the same force applied over a smaller area results in a higher pressure (pressure = force/area). The diamonds are aligned on a smoothly polished backing plate with an aperture for optical access to the sample through the diamond, and then secured with epoxy. Usually the backing plate is made from a strong material like tungsten carbide, but other specialty materials for various other applications can be used, such as copper beryllium for nonmagnetic purposes or beryllium for X-ray transparency. If a DAC is meant for reaching pressures higher than about 20 GPa, one backing plate will usually rest on a hemispherical rocker with tilt correction that allows the diamond faces to be aligned as parallel as possible. Aligning the two diamond culets in the two halves of the cell body and tightening the two halves together with screws apply force. Typically this is done by hand, with screws that have alternating left and right handed treads to prevent torque effects on the diamond culets. However, mechanical screw drives or gas membranes are often used for remote pressurization in synchrotron hutches or inside cryostats.

The sample chamber itself is made by pre-indenting a metallic gasket, usually about 250  $\mu\text{m}$  starting thickness, between the diamonds to a thickness of about 50  $\mu\text{m}$ , then drilling a hole inside the gasket of about half to two-thirds of the culet diameter. The gasket material is usually a hard malleable metal, with rhenium often used for the highest pressures and common steel being sufficient for lower pressures below 50 GPa. Pure beryllium, though relatively soft and brittle, is also often used when it is necessary to send X-rays through the gasket, as its X-ray absorption coefficient is extremely low compared to other metals. Specially machined flared gaskets are needed when this is done to ensure that the beryllium gaskets do not split during pre-indenting. Diamond or cubic boron nitride powder mixed with epoxy is also sometimes used when electrical insulating or non-magnetic materials are needed. The method of drilling the hole for the sample chamber varies with material, with mechanical drills, electron discharge machines, and even laser beams being used. Once drilled, the gasket is secured to one half of the DAC, and then the sample is loaded in the chamber with a manometer for measuring the pressure *in situ*. The chamber is finally flooded with a pressure transmitting medium (PTM), then both halves are brought together sealed. Friction between the gasket and diamond faces prevents the sample chamber from flowing out from between the two diamonds.

A PTM is needed to translate the uniaxial pressure from the opposed diamonds into hydrostatic pressure. All PTMs eventually solidify and become non-hydrostatic, creating often undesirable strain in the sample, but the best PTMs remain quasi-hydrostatic long after they have begun to solidify. Liquid media that can be loaded at room temperature are generally the easiest to work with, requiring no special equipment to load by hand, though one has to be careful not to wash the sample out of the sample chamber while loading. Two of the most widely used liquid PTMs are a mixture of 4:1 Methanol:Ethanol (ME) and Silicone oil. Both undergo a glass

transition at fairly low pressure (below 2GPa) but remain almost hydrostatic up to about 20 GPa [74], and both are fairly nonreactive. The 4:1 ME mixture is the slightly better PTM of the two at low pressures and room temperature, but is volatile and evaporates quickly. The more stable silicone oil is easier to work with overall, and at cryogenic temperatures is actually a better PTM above 20 GPa [75]. For higher pressures, no PTM is superior to gas mediums, most notably Neon and Helium. Neon freezes at about 5 GPa and begins to show strain at 16 GPa, while Helium freezes at 12 GPa and remains quasi-hydrostatic until over 60 GPa, but both degrade very slowly afterwards and are always better than any liquid medium. Neon shows diffraction peaks after solidifying which must be accounted for if doing XRD measurements, but the lighter Helium does not generally have this problem. Loading gas mediums require either using cryogenic liquids or high pressure filling, which both present their own problems. Cryogenic liquids are very volatile, can be dangerous to use, and presents the same sample positioning problems as using liquid media. High-pressure gas loading systems, such as the one at GSECARS in beamline 13 at the Advanced Photon Source [76], are very complex and labor intensive to maintain. They pressurize gas until it becomes a supercritical fluid and allows the cell to be mechanically sealed from outside the pressure chamber while allowing sample positioning to be undisturbed. Also, many such systems cannot be used with hazardous substances unless they were specifically built for such things. In general, it is best to use the least complicated method needed in order to maintain hydrostatic conditions over your desired range, but considerations to the sample you are working with often limit the type of loading you can use.

There are two common methods of measuring pressure inside a DAC. If XRD is available, gold powder or some other material with a well known equation of state can be put



inside the sample chamber along with the sample and the measured known diffraction pattern is used as a calibrant. However, this requires access to X-rays from a synchrotron or some similarly strong source. While convenient if XRD in the DAC is already being done, this is not useful for other types of measurements. The second method takes advantage of the optical clarity of the diamond anvils to measure the shift in wavelength of the R<sub>1</sub> fluorescence line of a piece of ruby in the sample chamber [77]. This can be done with a tabletop spectrometer along with a diode laser of lower wavelength or focused high intensity light source setup in any lab, such as the online ruby spectrometer at HPCAT 16-IDB at the Advanced Photon Source shown in Figure 24, which is similar to the example diagram in Figure 25. A good equation for the translating the ruby wavelength to absolute pressure up to 80 GPa is given by [78]:

$$P = \frac{A}{B} \left[ \left( \frac{\lambda}{\lambda_0} \right)^B - 1 \right] (GPa) \quad \text{Equation 13.}$$

where the fitted parameters  $A= 1904$  and  $B= 7.665$ , and  $\lambda_0 = 694.24$  nm is the zero-pressure value at 298 K. As the pressure medium becomes more non-hydrostatic, the ruby spectra will tend to become broader, giving a good qualitative indication of rising strain in the sample chamber.

## Chapter 2: Experimental Procedure

### *Cerium Samples*

Single crystals of  $\text{CeCu}_2\text{Ge}_2$  and  $\text{CeCoSi}$ , synthesized using a metallic flux method as described elsewhere [79], were obtained from the Condensed Matter and Thermal Physics Group (MPA-10) at LANL. The crystals were ground into a fine powder and passed through a  $5\ \mu\text{m}$  sieve. For ambient pressure measurements, a thin layer of powder was brushed between layers of cellophane tape. For high-pressure measurements, the sample was mixed with silicone oil in about a 7:1 oil to sample ratio by weight. This oil/sample mixture served the dual purpose of creating a uniform material of proper absorption length and acting as a pressure-transmitting medium inside the diamond anvil cell (DAC). The mixture was refined using trial and error by mounting it in the cell at near ambient pressure and then testing it in the beam until an edge step near unity was achieved. A CuBe DAC with a built in gas membrane drive was used, manufactured by Almax-EasyLab, shown in Figure 26. The Ce  $L_3$  edge ( $\sim 5.7\ \text{keV}$ ) is low enough in energy that diamond begins to significantly absorb X-rays at this energy, with an absorption length of about only  $300\ \mu\text{m}$ , as seen in Figure 27. Because of this, it was desirable to reduce the amount of diamond that the beam must travel through so that the maximum amount of absorption was due to the Ce in the sample. To accomplish this, a combination of a diamond anvil partially perforated down to  $100\ \mu\text{m}$  wall thickness and a micro-diamond about  $500\ \mu\text{m}$  high mounted on a fully perforated diamond backing anvil were used as in figure 28. The micro-diamond arrangement allowed optical access to the sample chamber, where fluorescence of a ruby chip inside was used to determine the pressure, according to a standard ruby pressure scale [77]. To make the sample chamber, a rhenium gasket was pre-indented to  $50\ \mu\text{m}$  between the  $300\ \mu\text{m}$  culets of the diamond anvils. A  $200\ \mu\text{m}$  hole was laser drilled in the gasket indentation,

into which the sample/oil slurry and ruby chip were then loaded. The flat, well aligned faces of the diamonds also provided for a uniform thickness of the sample over the area of the X-ray beam.

High pressure XANES was performed on the Ce  $L_3$  edge of the samples at beamline 4-ID-D at the Advanced Photon Source (APS), Argonne National Laboratory. Transmission geometry through the perforated diamond anvils was used, and diodes were used to measure the incoming and outgoing flux from the DAC. The synchrotron radiation beam spot was focused by a Pd toroidal mirror and slit to about an area of  $30 \times 30 \mu\text{m}^2$ . In order to avoid diamond glitches caused by Bragg diffraction from the single crystal diamond anvils, the DAC was rotated small angles in a plane perpendicular to the x-ray beam until no undesired features were seen in the spectra as the incoming beam energy was scanned across the Ce  $L_3$  edge energy.

In order to reach 10 Kelvin, a liquid helium flow cryostat with sapphire windows for optical access was used. Instead of screws, pressure in the DAC was remotely regulated using a helium gas membrane drive similar to that shown in purple in the cutaway in Figure 29. The thin membrane is actually two steel ring shaped discs welded together that inflate slightly as helium is pumped into it at up to 3000 psi, using a regulator similar to Figure 30. Pressure was measured *in situ* using ruby fluorescence. Once down to lowest temperature, pressure was increased in steps up to 20 GPa for CeCu<sub>2</sub>Ge<sub>2</sub> XANES measurements were taken, then again as pressure was released. Lower pressures below 7 GPa were unable to be obtained for CeCu<sub>2</sub>Ge<sub>2</sub> as thermal contraction of the DAC would cause an increase in pressure during the cooling process which could not be relieved while the DAC was inside the cryostat. For CeCoSi, XANES measurements were taken at multiple temperatures: 12K, 100K, and 200K up to 11 GPa. Multiple scans, usually 5 to 7, were taken at each pressure step, then these were averaged

together in order to account for slight variations in beam position over a single measurement. An energy range from 50 eV below to 100 eV above the cerium  $L_3$  edge at 5.72 keV was taken, using 0.5 eV steps.

Powder XRD measurements on CeCoSi were performed in a DAC using silicone fluid as the quasi hydrostatic pressure medium. For single crystal XRD measurements, small single crystal specimens were cleaved from the larger polycrystalline aggregate and were loaded in a specially designed DAC with He as a hydrostatic pressure transmitting medium with a wide opening to allow a  $45^\circ$  angle sweeps to improve the accuracy. Small annealed ruby spheres (<5  $\mu\text{m}$  diameter) were used for pressure determination using standard ruby fluorescence measurements [8]. Diffraction experiments were conducted at 16-IDB at the HP-CAT sector 16 of the Advanced Photon Source and at beamline 12.2.2 at the Advanced Light Source. The GSE-ADA RSV software package for peak fitting, integration, and indexing [81].

### *Uranium Samples*

Single Crystals of uranium samples  $\text{UCd}_{11}$ ,  $\text{UCu}_2\text{Si}_2$ , and  $\text{U}_3\text{Ni}_5\text{Al}_{19}$  were synthesized by similar self-metallic flux methods [11, 38, 82] and obtained from the same group, the Condensed Matter and Thermal Physics Group (MPA-10) at LANL. Samples were mixed in a ratio with an overabundance of flux: Cd, Si, or Al. They were then sealed in an alumina crucible sealed under vacuum in a quartz tube, heated to over 1100  $^\circ\text{C}$  and kept there for several hours, and then slowly cooled to an intermediate high temperature where the excess flux was separated from the crystals using a centrifuge.

High-pressure uranium  $L_3$  edge X-ray absorption spectra in partial fluorescence yield mode (PFY-XAS) were taken on HPCAT 16-ID-D undulator beamline at the Advanced Photon

Source (APS). A monochromatic X-ray beam was obtained using a Si (111) double crystal monochromator, focused to a beam size of  $25 \times 55 \mu\text{m}^2$  with meter-long horizontal and vertical Kirkpatrick-Baez mirrors. For ambient temperature measurements, a Paderborn-panoramic style diamond anvil cell (DAC), equipped with Boehler-Almax anvils of  $300 \mu\text{m}$  culet diameter and a beryllium gasket, was used to apply high pressure, similar to that in Figure 31. For low temperature measurements, a Princeton Moa-type symmetric cell was loaded in a helium flow cryostat with Kapton windows using a gas membrane drive, also with a beryllium gasket, similar to Figure 32. The beryllium gasket was pre-indented to  $50 \mu\text{m}$  thickness and a  $100 \mu\text{m}$  diameter hole was drilled to serve as a sample chamber. Annealed ruby spheres of  $\sim 5 \mu\text{m}$  diameter were placed in the gasket hole along with the sample as a pressure calibrant. Samples about  $\sim 30 \mu\text{m}$  thick were used: single crystal flakes for  $\text{UCd}_{11}$ , and polycrystalline flakes for  $\text{U}_3\text{Ni}_5\text{Al}_{19}$  and  $\text{UCu}_2\text{Si}_2$ . A 4:1 methanol-ethanol mixture was loaded as a pressure-transmitting medium for room temperature measurements, and silicone oil was used for all low temperature measurements. Radial scattering geometry was employed, where the incoming X-ray beam entered through the Be gasket in the radial direction and the secondary emission from the sample passed through the Be gasket to the spectrometer analyzer, as shown in Figure 33. Inside the cryostat, due to space limitations, the incoming X-ray beam was directed through a diamond, but the X-ray intensity was not attenuated enough to be an issue. Due to safety regulations ambient data was not taken on the same sample inside the pressure cell. Therefore a separate sample of  $15 \mu\text{m}$  thickness was used to take ambient PFY-XAS data in an aluminum gasket, double sealed with Kapton tape. A Rowland circle spectrometer was used to analyze the secondary emitted fluorescence beam from the sample.

The spectrometer was comprised of a spherically bent Si (844) single crystal analyzer and Peltier-cooled silicon detector (AMPTEK XR\_100CR). The spectrometer utilized the Rowland circle geometry where the sample, the single crystal analyzer (1 meter bend radius) and the detector all lie on the perimeter of the Rowland circle with a diameter of 1 meter. For PFY-XAS measurements, the intensity of the U  $L_{\alpha 1}$ , ( $3d_{5/2} - 2p_{3/2}$ ) (13.614 keV) fluorescence line is measured as a function of the incident photon energy varied from 20 eV below to 50 eV above the U  $L_3$  absorption edge (17.166 keV). The acquisition time for each PFY-XAS spectrum at a given pressure was about 20 minutes. The energy resolution of the incoming beam was about 2.2 eV and the spectrometer energy resolution was about  $\sim 0.7$  eV, giving a total estimated energy resolution of 2.3 eV. The sample was aligned to minimize self-absorption. Ideal sample size for XAS measurements in fluorescence mode should be either sufficiently thin or dilute to avoid self-absorption from the outgoing emitted beam [83]. The sample inside the pressure cell was 30  $\mu\text{m}$  thick whereas the sample used for ambient data was 15  $\mu\text{m}$  thick. Although corrections for self-absorption effects exist in the thick limit, our samples were too thin to be considered in the thick limit; that is, they are in the intermediate thickness limit where correction factors do not currently exist. Consequently, there is no way to correct the in-cell data and the out-cell data. However, although the two samples differ in thickness by 15  $\mu\text{m}$ , a comparison between the data for  $\text{UCd}_{11}$  from the two samples and with the data in Ref [11] is reasonably good. Note that this correction is important primarily for comparing the ambient pressure data to the applied-pressure data sets.

High pressure single crystal X-ray diffraction (XRD) measurements at room temperature were taken on  $\text{UCd}_{11}$ , using a four-post wide-opening DAC equipped with Boehler-Almax diamond anvils of 600  $\mu\text{m}$  culet diameter and a  $70^\circ$  aperture, similar to Figure 34. A single

crystal of  $\text{UCd}_{11}$  ( $100 \times 120 \mu\text{m}^2$ ) was loaded into a rhenium (Re) gasket with pre-indented thickness of  $70 \mu\text{m}$  and a  $200 \mu\text{m}$  diameter drilled hole. Two annealed ruby spheres of  $\sim 5 \mu\text{m}$  diameter were placed in the gasket hole along with the sample as a pressure calibrant. A 4:1 methanol-ethanol mixture was loaded as a pressure-transmitting medium in the DAC just as in the XANES measurements. The data was collected at the HPCAT 16-ID-B undulator beamline at APS, at a range from 0-20 GPa in the angular dispersive mode with a monochromatic X-ray beam of  $\lambda = 0.4066 \text{ \AA}$  from a Si (111) double crystal monochromator. The diffraction patterns were collected using a MAR CCD, which was calibrated using a  $\text{CeO}_2$  standard through Fit2D software [68]. At each pressure a wide scan in  $\omega$  in the range  $\pm 38^\circ$  as well as a step scan of  $1^\circ$  interval in the same angular range was taken. Each wide scan was also split into 4 intervals of  $19^\circ$  for better statistics. GSE\_ADA software [85] was utilized to extract the two peak coordinates, integrated intensities,  $2\theta$  and the azimuthal angle ( $\chi$ ) around the beam from the  $\pm 38^\circ$  wide scan. The stepped scans were used to extract the maximum intensity at each angle and the third spatial coordinate ' $\omega$ ' which contains information needed to reconstruct the reciprocal space and index the diffraction pattern. Lorentz and polarization corrections were applied to the fitted peaks using GSE\_ADA software. The refinement of the orientation matrix, lattice parameters and the reconstruction of reciprocal lattice were done using the RSV software [85]. For structure analysis in GSE\_ADA, saturated peaks, overlapped peaks, diamond peaks and peaks at the edge of the wide scan range in  $\omega$  were not considered. Absorption by the crystal was negligible and so was not considered.

High-pressure powder XRD was taken on  $\text{U}_3\text{Ni}_5\text{Al}_{19}$  at room temperature again at HPCAT 16-ID-B at APS, using a Princeton Mao-type symmetric cell with  $400 \mu\text{m}$  culet diamonds. A rhenium gasket was pre-indented to  $50 \mu\text{m}$  and drilled with a  $200 \mu\text{m}$  hole. A

polycrystalline 50  $\mu\text{m}$  flake of  $\text{U}_3\text{Ni}_5\text{Al}_{19}$  was loaded in the sample chamber with 4:1 methanol-ethanol used as a pressure medium and a  $\sim 5 \mu\text{m}$  annealed ruby sphere for pressure measurement. Powder XRD was performed in angle dispersive mode at pressures up to about 37 GPa, using an X-ray beam of  $\lambda=0.40662 \text{ \AA}$  with area about  $10 \times 15 \mu\text{m}$ , also using a  $\text{CeO}_2$  calibrant.



## Chapter 3: Results

### *Cerium Compounds*

Figure 35. shows the evolution of the CeCu<sub>2</sub>Ge<sub>2</sub> L<sub>3</sub> edge with pressure from ambient to 20 Gpa. It begins with only a single peak at ambient pressure, but the peak at about 5.737 keV can clearly be seen growing with pressure. Each spectrum can be deconvoluted as a combination of an edge jump (arctangent normalized to unity) and two distinct peaks – corresponding respectively to electronic f<sup>0</sup> (tetravalent Ce<sup>4+</sup>) and f<sup>1</sup> (trivalent Ce<sup>3+</sup>) configurations of the cerium atom. As pressure increases we observe a clear increase in f<sup>0</sup> spectral weight, while the f<sup>1</sup> component decreases continuously in intensity. Taken together, these changes suggest a valence moving from a nearly Ce<sup>3+</sup> state towards a more Ce<sup>4+</sup> configuration – consistent with an increased delocalization of the Ce 4f electrons in the high pressure phase. This is mirrored in all the CeCoSi spectra as well, as seen in Figure 36 using the lowest temperature data as an example.

We can calculate the cerium valence by using a phenomenological approach which has been successfully applied in the case of metallic intermediate valence compounds. In this approach, the two white lines of the L<sub>3</sub> edge spectrum are simply interpreted as f<sup>1</sup> and f<sup>0</sup> final states, and the average valence is simply obtained from the relative intensities of the two edges. The determination of the valence using this method on CeCu<sub>2</sub>Ge<sub>2</sub> at 14.3 GPa and 10 K as an example is shown in Figure 37. All analysis of XANES data was done with Ravel and Newville's Athena using IFEFFIT [84]. A pseudoVoigt function is used for the peaks, in an attempt to satisfy the Lorentzian profile of the core-hole lifetime broadening and the Gaussian instrumental broadening, which are about the same order of magnitude for the cerium L<sub>3</sub> edge in this experimental setup. The fractional valence can then be calculated as:

$$V = 3 + \frac{I_{4+}}{I_{3+}+I_{4+}} \quad \text{Equation 14.}$$

where  $I_{3+}$  and  $I_{4+}$  are the intensities of the white lines corresponding to the  $Ce^{3+}$  and  $Ce^{4+}$  states respectively. There are clearly no discontinuities in the measured valence versus pressure plots as seen in Figures 38 and 39. Specifically, the lack of a sudden large valence discontinuity seen at 16 GPa in  $CeCu_2Ge_2$  puts doubt as to whether the Volume collapse seen by Onodera *et al.*[30] was real, though this is not unexpected as more recent measurements have already put that into question [32]. More surprisingly, there is also no noticeable effect on the  $CeCoSi$  data as the system goes through the  $T_v$  transition for  $CeCoSi$ . However, this lack of a discontinuity is similar to the results on the  $CeCu_2Ge_2$  sample and  $CeCu_2Si_2$  from Rueff *et al.* [86]. The  $CeCoSi$  valence also seems to show little to no effect due to temperature within the experimental accuracy, as all curves seem to coincide in Figure 39.

Comparing the  $CeCu_2Ge_2$  valence data directly to literature measurements of  $CeCu_2Si_2$  [86] gives some more insight into the process behind the superconducting state. In Figure 40, the values of the pressure scale are adjusted to  $P - P_c$  for both compounds, where  $P_c$  is the pressure where the superconducting transition temperature ( $T_c$ ) is at its maximum. Doing this shows an overlap of the valences, crossing at exactly zero converted pressure, corresponding to the pressure at which the QCP is expected to occur. This makes it appear that value for the fractional valence the cross happens at, about 3.1, is a threshold for some sort of slow first order valence transition.  $CeCu_2Ge_2$  is more compressible than  $CeCu_2Si_2$  so the curves do not line up in Figure 40. In order to investigate the effect of cell volume, instead of scaling by pressure on the x-axis, the XRD data from Kobayashi *et al.* [32] was used to convert pressure to unit cell volume

for both compounds, and valence was converted to average f electrons per Ce site ( $\bar{n}_f$ ) using a weighted sum of the f states and:

$$\bar{n}_f = \frac{1}{2}n_f = \frac{1}{2}[(f^0 \text{ peak area}) * 0 + (f^1 \text{ peak area}) * 1] \quad \text{Equation 15.}$$

This shows an even better agreement between the two analogous compounds in Figure 41.

The single crystal X-ray diffraction (SXRD) measurements in a hydrostatic He pressure medium confirm the stability of the low-pressure tetragonal P4/nmm structure for the CeCoSi from ambient conditions up to about 4.5 GPa. However, above 4.5 GPa, changes in the XRD pattern where new diffuse spots appear indicate a discontinuous transition to a distorted high-pressure phase, shown in the raw XRD image in Figure 42. The most important change observed is the formation of a superlattice-type structure in the high pressure phase via the tripling of the c-lattice parameter,  $c' = 3c$ , shown in Figure 43. This results in reduction of the Brillouin Zone, and is likely related to the emergence of a charge density wave (CDW) state in the high pressure phase that is incommensurate with the original unit cell length  $c$ , that would in turn impact the electronic occupancy of the cerium. The emergence of superconductivity around the same 4.5 GPa pressure would strongly suggest that the valence state changes drive the superconducting transition in this compound.

Based on the reflections observed, the high-pressure phase is indexed to a weakly distorted P4/nmm structure. The distortion occurs mainly along the  $a$  lattice parameter. As a result of this discontinuous distortion, the beta angle in the high pressure phase changes from  $90^\circ$  in the ambient pressure phase, to  $90.5-93.5^\circ$  in the distorted high pressure phase. The transition appears to proceed without any apparent volume discontinuity (within the precision of this study)

as shown in Figure 44. No other transitions were observed up to the maximum pressure of 10Gpa.

### *Uranium Compounds*

The XRD for both  $\text{UCd}_{11}$  and  $\text{U}_3\text{Ni}_5\text{Al}_{19}$  showed that the low pressure phases of both materials hold over the course of the experiment, with no phase transitions as the crystal lattices were contracted, seen in Figures 45 and 46. Table 1 and Table 2 give the parameters for fits to the Birch–Murnaghan EOS and Vinet EOS fits, showing  $\text{UCd}_{11}$  to be very compressible with a relatively low bulk modulus, but otherwise no notable or unexpected features. A previous study confirmed the phase stability of  $\text{UCu}_2\text{Si}_2$  up to 10 GPa at least [50].  $\text{UCd}_{11}$  showed the highest relative compression to the other uranium compounds, with a 6.3% reduction in the interatomic U-U distance, but none of the them are compressed below the Hill limit. This rules out structural transitions as cause for the electronic changes measured in the XANES experiments.

The XANES data for all the Uranium compounds are shown in Figures 47 through 52. Peaks were fitted to the XANES spectra using the Athena software package with the same methods as the cerium compounds, only no individual peaks were assigned to the different valence states. Instead one pseudo voight function fitted along with a normalized arctangent function to account for the edge step was used. The valence data show a relatively modest but significant increase in the whteline energy, with a  $\Delta E = 1\text{eV}$  for the  $\text{U}_3\text{Ni}_5\text{Al}_{19}$  sample and  $\Delta E = 1.3\text{eV}$  for the  $\text{UCu}_2\text{Si}_2$ .  $\text{UCd}_{11}$  however, shows a very large increase of 4.1 eV over its pressure range. In comparison to Figure 3, this indicates a change in f electron occupancy of 1 whole electron. This is not explained by a simple linearly proportional change in the interatomic U-U distance compared to the other compounds. The wave functions of the uranium f electrons do

not overlap significantly at this spacing, so  $5f-4d$  hybridization is likely the dominant control parameter for the formation of the ground state as the U-Cd interatomic distance is reduced.

## Chapter 4: Conclusions

The XANES spectra of heavy-fermion materials  $\text{CeCu}_2\text{Ge}_2$ ,  $\text{CeCoSi}$ ,  $\text{UCu}_2\text{Si}_2$ ,  $\text{U}_3\text{Ni}_5\text{Al}_{19}$ , and  $\text{UCd}_{11}$  were measured to high pressures using a combination of transmission and fluorescence geometries. This was used to directly probe the valence state at the cerium and uranium sites in their respective compounds as a function of pressure. These were correlated with structural XRD measurements of  $\text{CeCoSi}$ ,  $\text{U}_3\text{Ni}_5\text{Al}_{19}$ , and  $\text{UCd}_{11}$  made in this work and literature data for the others, and the bulk modulus from the equation of state was found for  $\text{U}_3\text{Ni}_5\text{Al}_{19}$  and  $\text{UCd}_{11}$ .

The lack of a valence discontinuity in  $\text{CeCu}_2\text{Ge}_2$  debunks the controversial existence of a volume collapse reported in Onadrea *et al.*[30] that was associated with a QCP. However, comparison with its isostructural analogue  $\text{CeCu}_2\text{Si}_2$  reveals that a change in valence is essential to the formation of that QCP and the onset of a superconducting state. A similar trend was found in  $\text{CeCoSi}$ , where magnetic resistance measurements showed evidence of a valence transition under pressure, but no valence discontinuity was seen. More work on these compounds using chemical substitution to further tune the disorder and pressure in them would be useful.

The change in energy of the white line peak with pressure in  $\text{UCu}_2\text{Si}_2$ ,  $\text{U}_3\text{Ni}_5\text{Al}_{19}$ , and  $\text{UCd}_{11}$  was used to measure the change in localization of the f electrons at the uranium sites. A particularly large  $\Delta E = 4.1$  eV for  $\text{UCd}_{11}$  is notable, as its large interatomic distance makes it very localized but a modest decrease has caused a large change in its f electron occupancy. As this is one of few heavy-fermion uranium materials where the f electron configuration at ambient pressure is well known from resonant X-ray emission spectroscopy (RXES), it would be a good candidate for further RXES measurements at high pressure.

Appendix: Figures

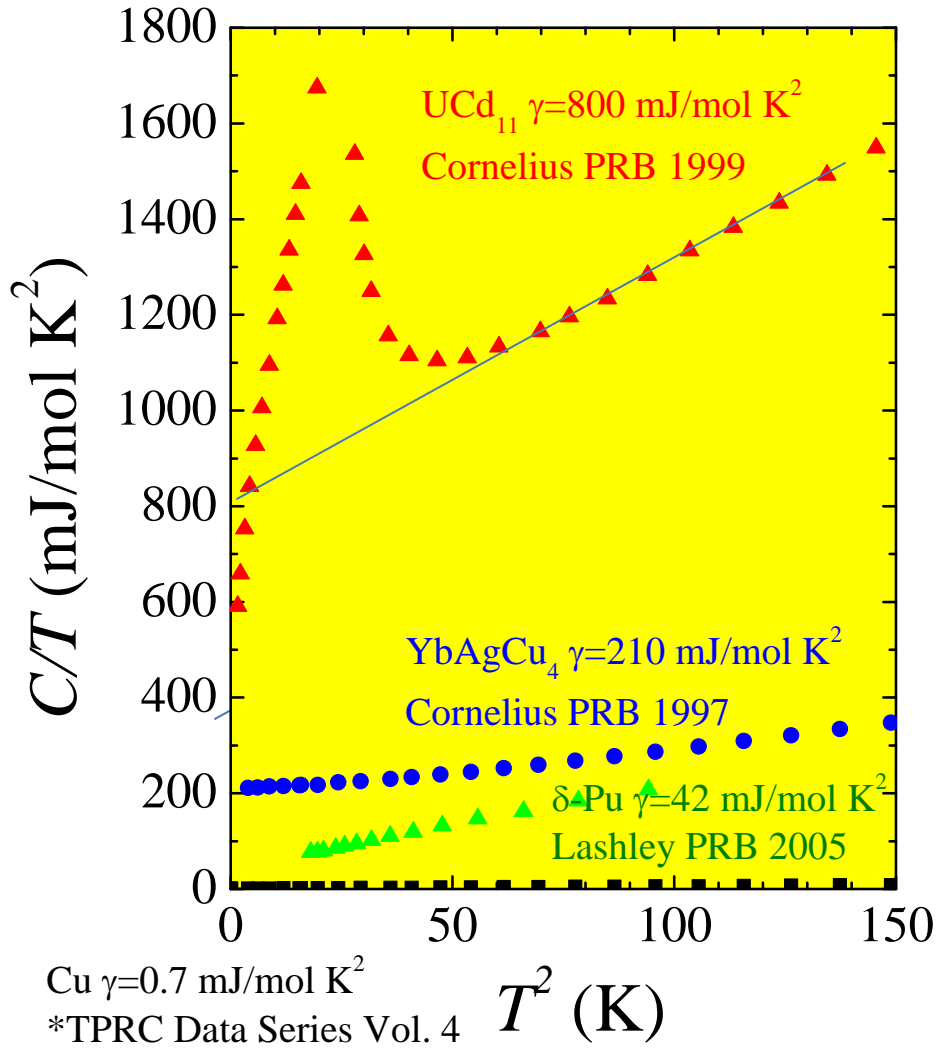



**Figure 1. Examples of Heavy-Fermion Materials with High Sommerfeld coefficients.** An extrapolation from higher temperatures is used for UCd<sub>11</sub> which has a low temperature magnetic feature.

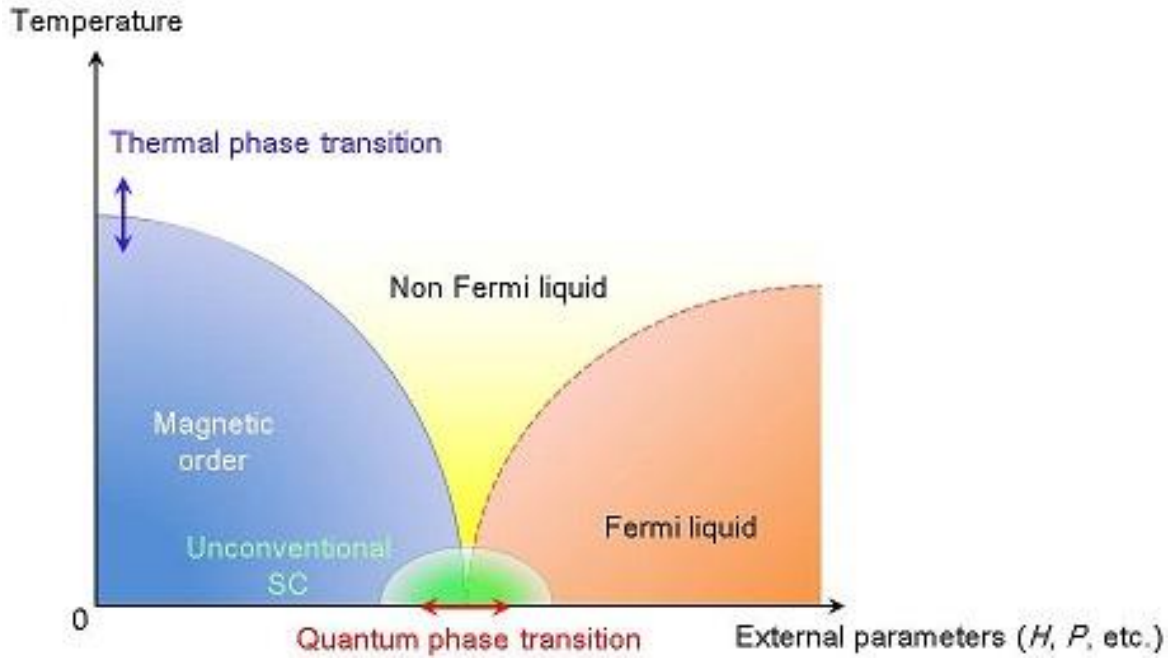


**Figure 2. Phase Diagram showing a QCP in a heavy fermion material.** There are many types of tuning parameters that can drive a transition to zero Kelvin and produce a QCP, from Tokiwa *et al.* [20]



Empty Shell	Partially Filled Shell												Full Shell		
	<b>Yb<sup>3+</sup></b>														
4f	La	<b>Ce</b>	Pr	Nd	Pm	Sm	Eu	Gd	Tb	Dy	Ho	Er	Tm	Yb	Lu
5f	Ac	Th	Pa	<b>U</b>	Np	Pu	Am	Cm	Bk	Cf	Es	Fm	Md	No	Lr
3d	Ca	Sc	Ti	V	Cr	Mn	Fe	Co	Ni	Cu	Zn				
4d	Sr	Y	Zr	Nb	Mo	Tc	Ru	Rh	Pd	Ag	Cd				
5d	Ba	La	Hf	Ta	W	Re	Os	Ir	Pt	Au	Hg				


**Increasing Localization**

**Figure 3. A modified periodic table showing trends in localization.** Strongly correlated electron behavior occurs in the transition area between localized and delocalized behavior, highlighted in yellow, adapted from Smith and Kmetko [87].

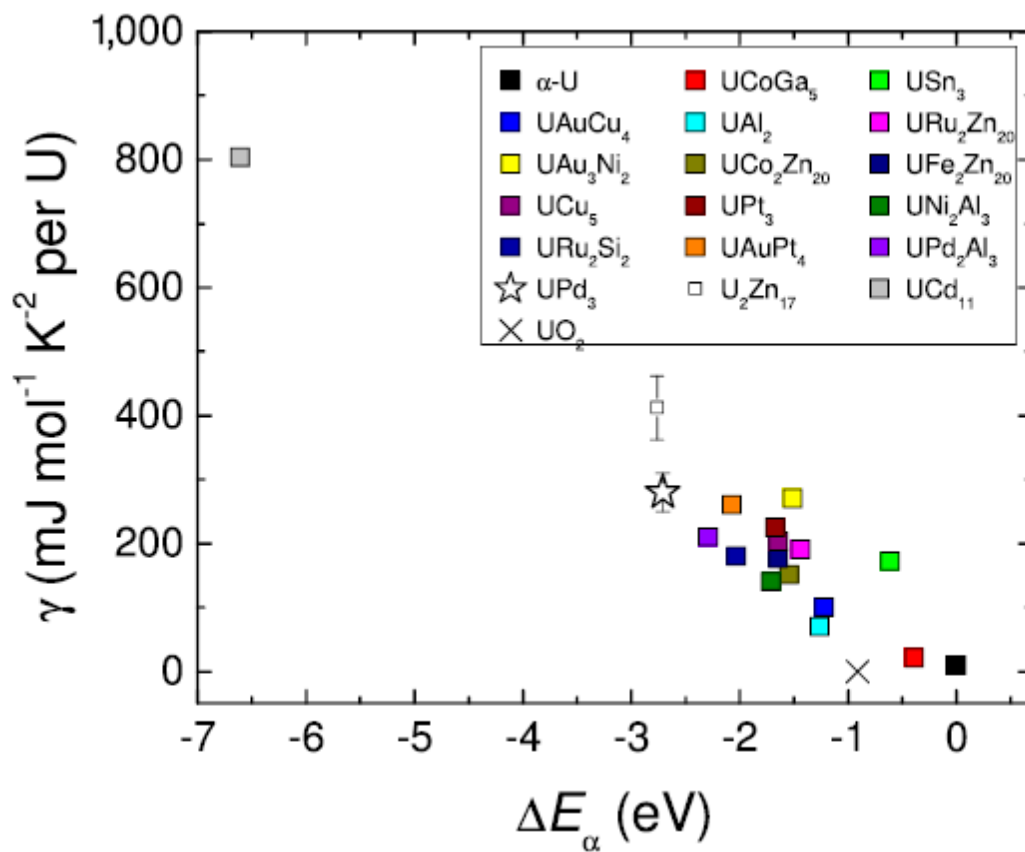


**Figure 4.** Plot relating energy shift of the L<sub>3</sub> edge to the Sommerfeld coefficient. A higher Sommerfeld coefficient corresponds to more localized f electron behavior [11].

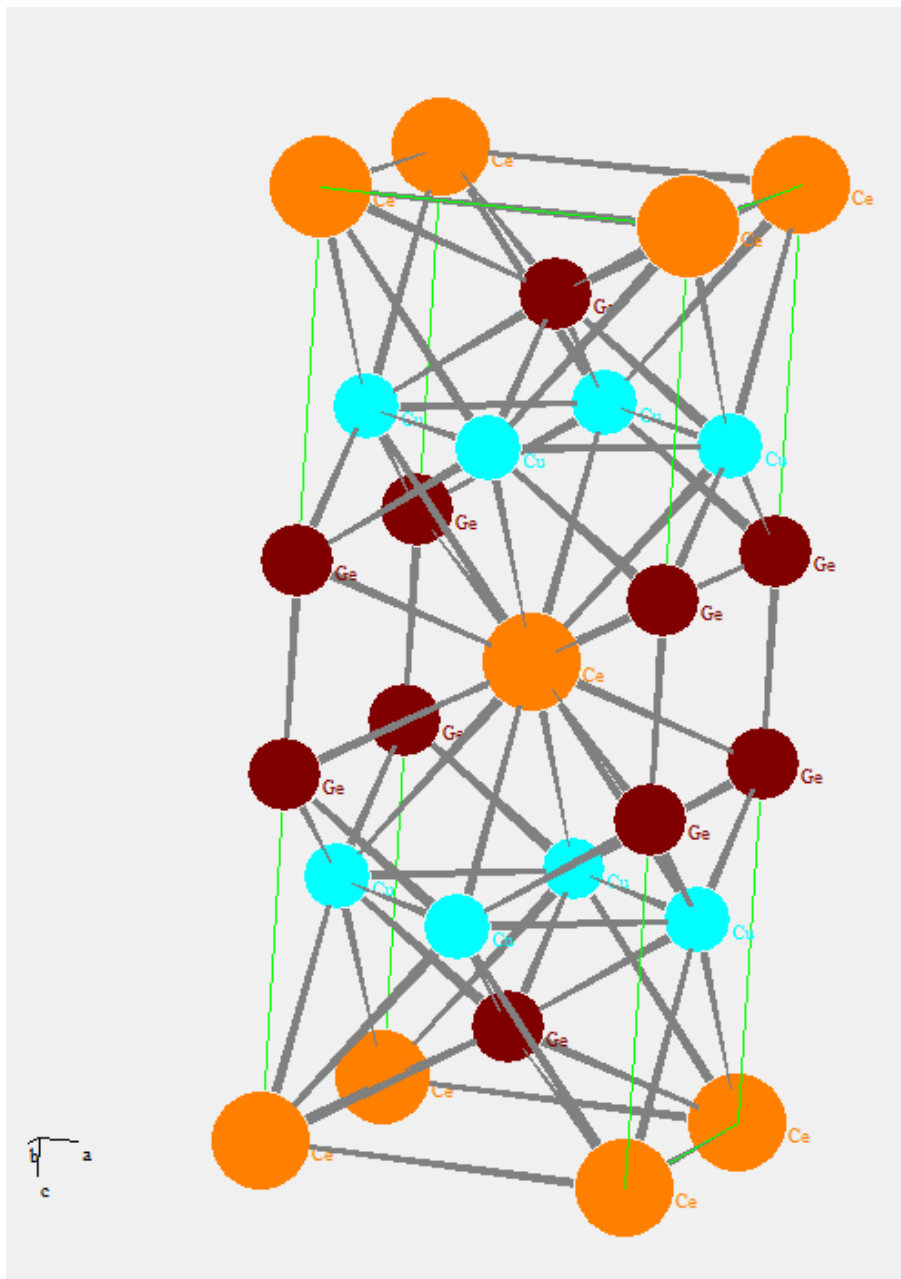


**Figure 5. Crystal structure of CeCu<sub>2</sub>Ge<sub>2</sub>.**

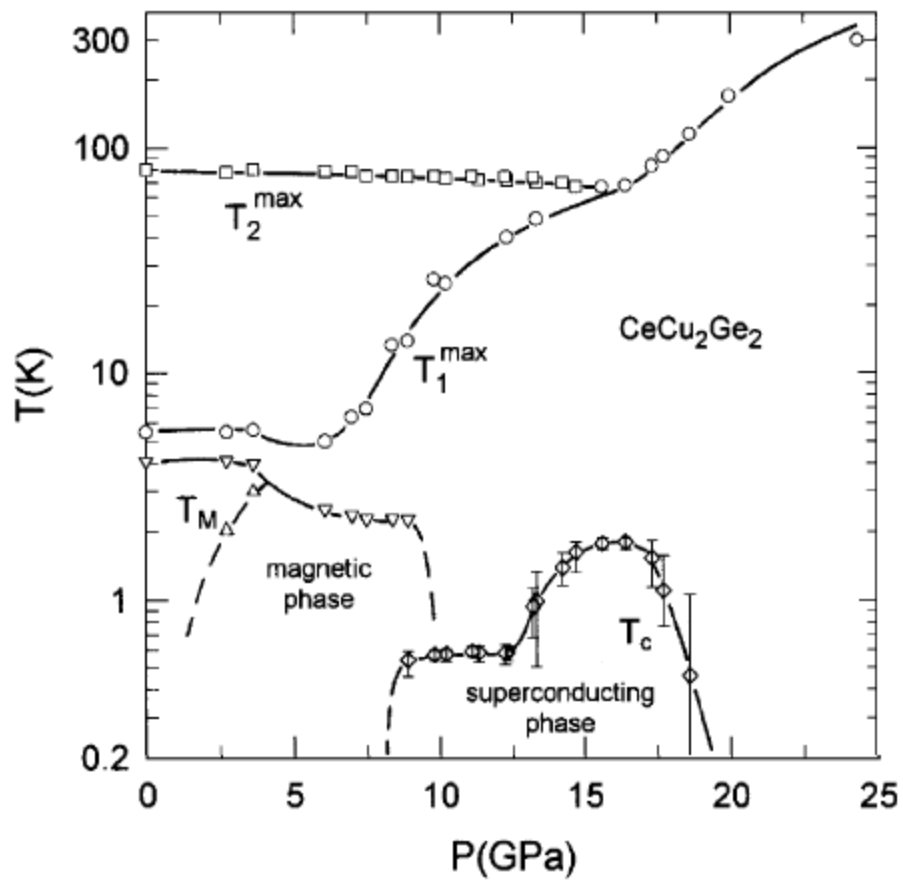


Figure 6. Phase Diagram of CeCu<sub>2</sub>Ge<sub>2</sub>. [24]

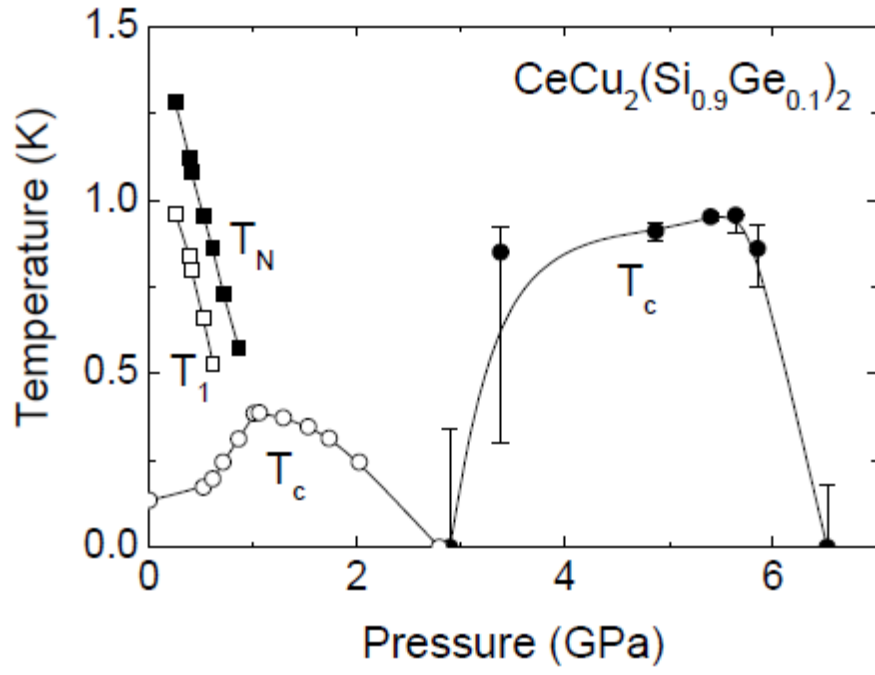


Figure 7. The Superconducting region split. [26]

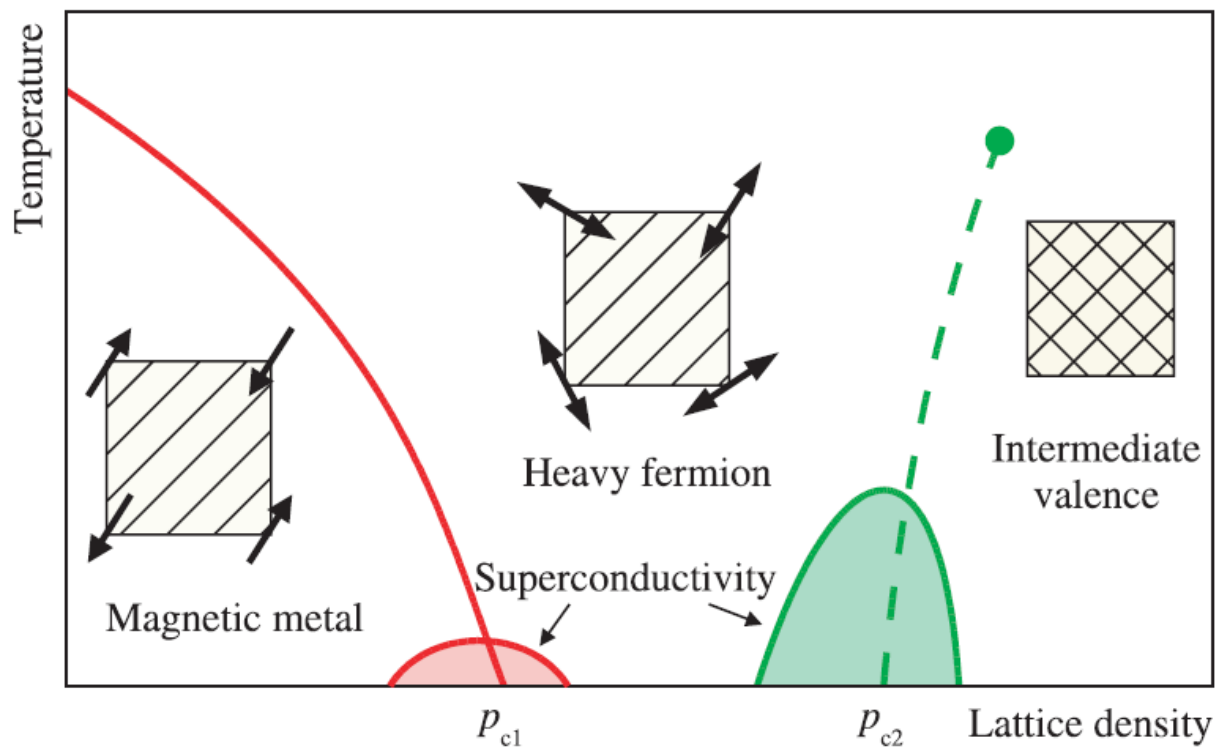
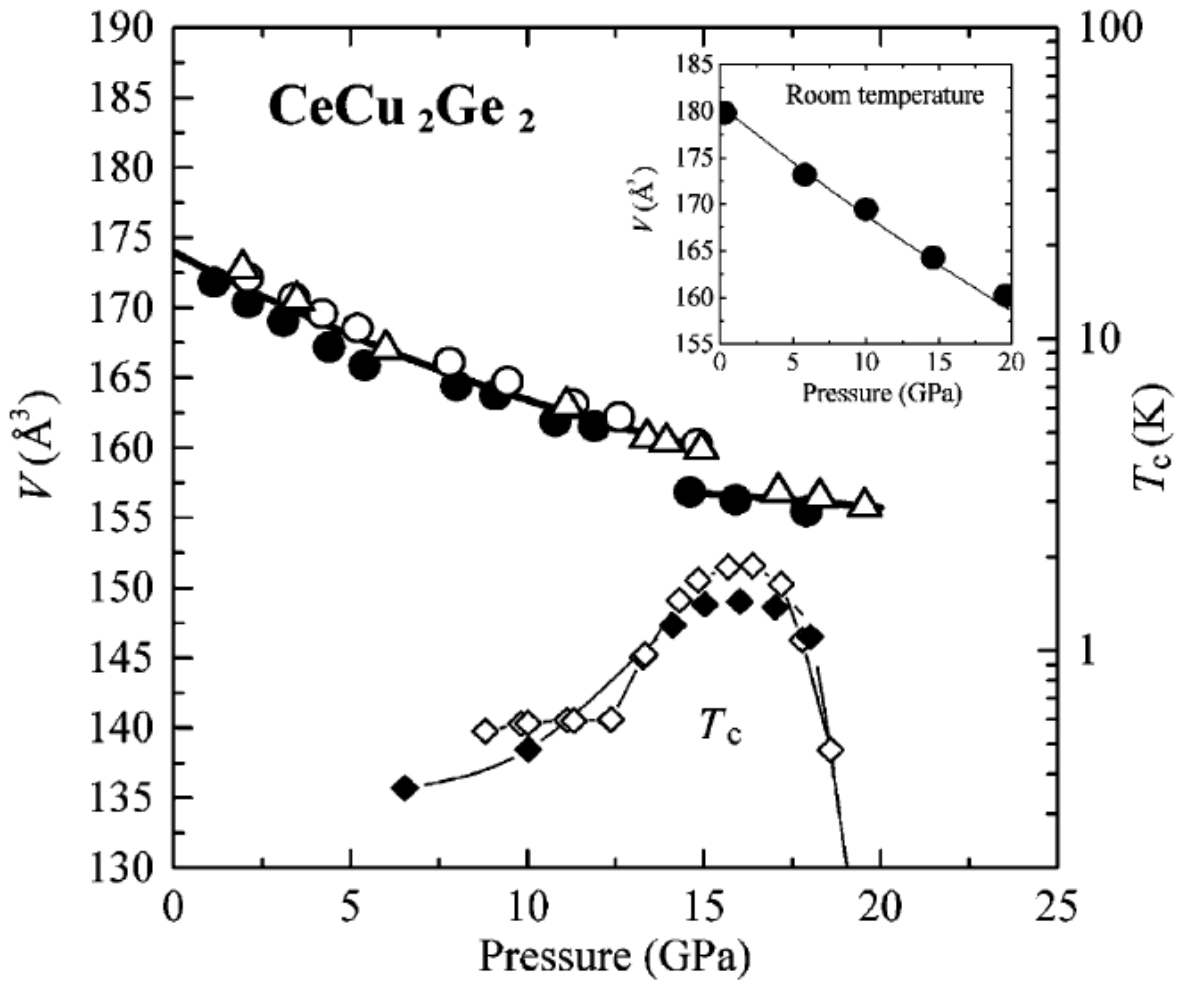
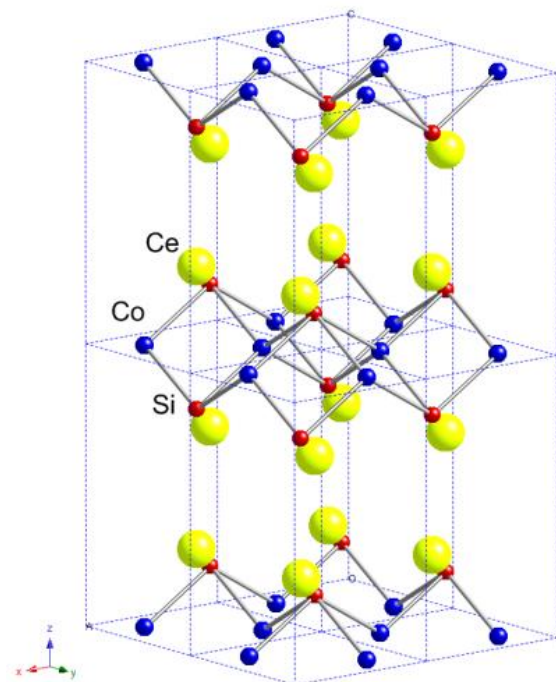


Figure 8. The two distinct superconducting phases in  $\text{CeCu}_2\text{Ge}_2$ . [27]



**Figure 9. Proposed isostructural volume collapse in CeCu<sub>2</sub>Ge<sub>2</sub>.** Equation of state of CeCu<sub>2</sub>Ge<sub>2</sub> at 10 K. Each symbol is from separate series of experiments [30]. The  $T_c$  data are from Kobayashi et al. [32] (closed diamonds) and Jaccard et al. [24] (open diamonds).



**Figure 10.** The crystal structure of CeCoSi. The shifted-layer structure presents opportunities for mixing between the Ce 4f orbitals and the Co 3d orbitals contributing to the complex electronic landscape observed in this compound.



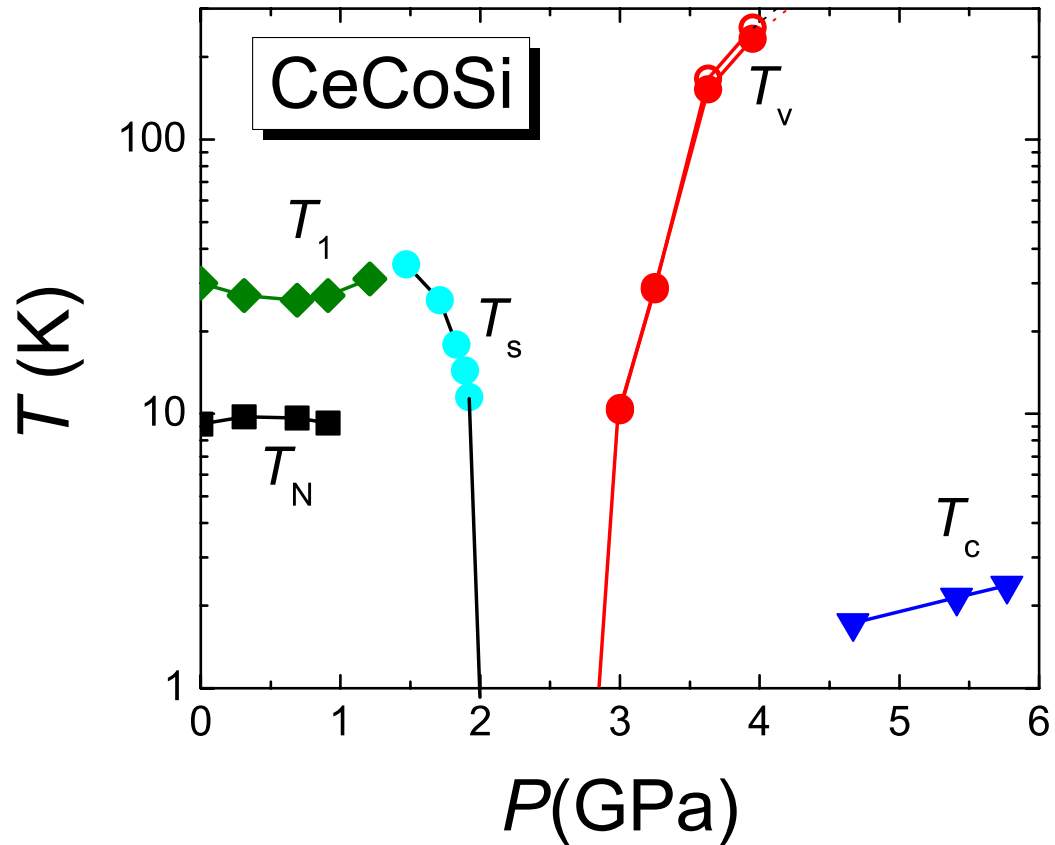


**Figure 11. Phase diagram for CeCoSi.** Determined by temperature dependent electrical resistance measurements [36]. Up to 2 GPa, magnetically ordered states are inferred from  $T_N$ ,  $T_1$  and  $T_S$ . From 3-4 GPa a first order transition consistent with a valence transition  $T_V$  is observed. Above 4.5 GPa, data consistent with the onset of superconductivity  $T_C$  is seen.

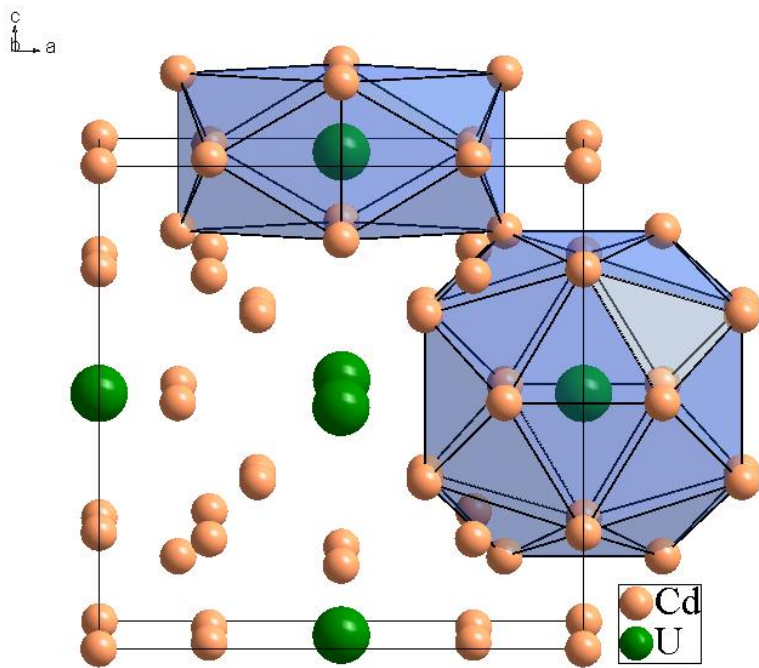


Figure 12. Crystal structure of  $UCd_{11}$ .

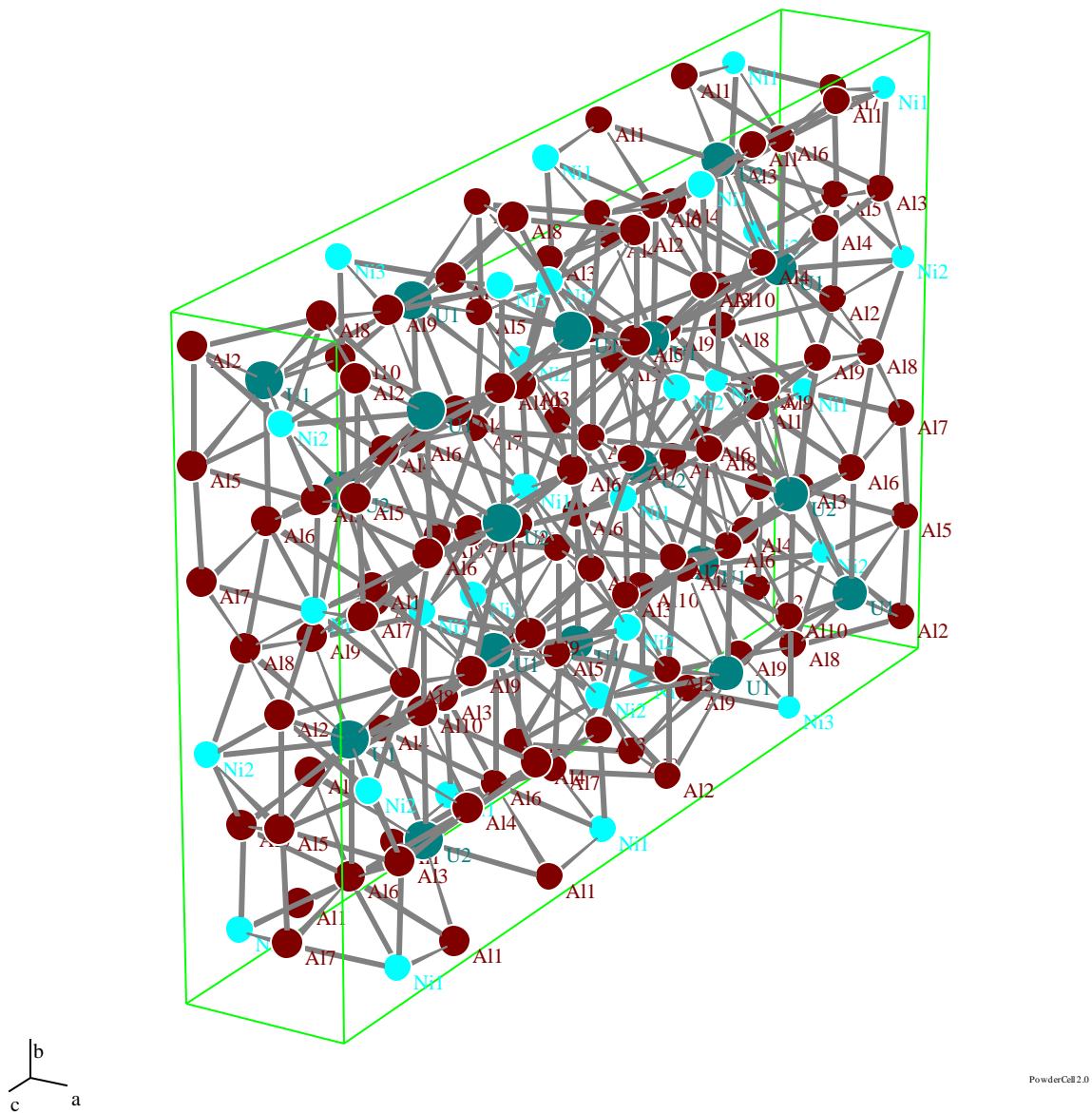
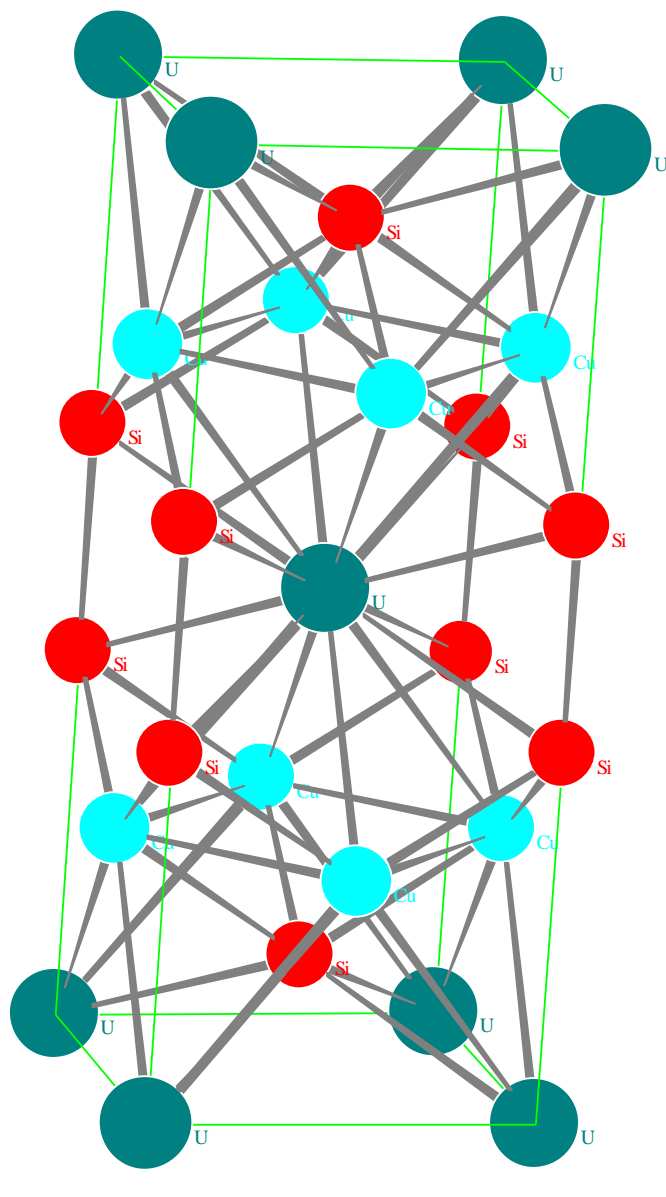
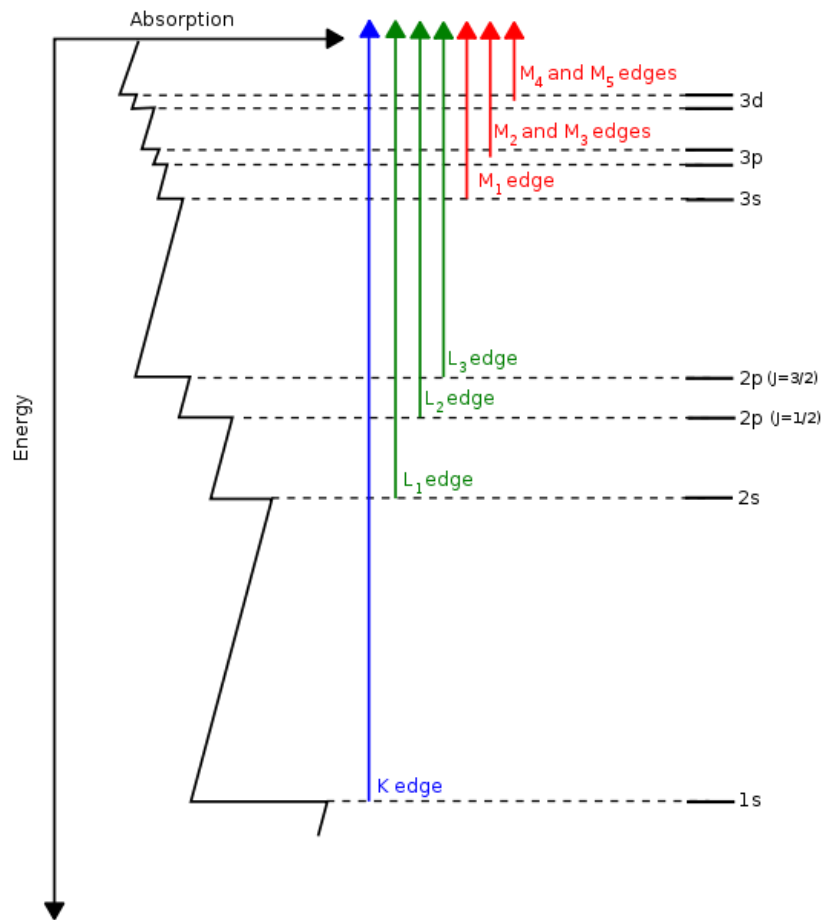


Figure 13. The crystal structure of  $U_3Ni_5Al_{19}$ .



**Figure 14.** The crystal structure of  $UCu_2Si_2$



**Figure 15. XAS Edges.** The  $L_3$  edge was used for all samples in these experiments [56].

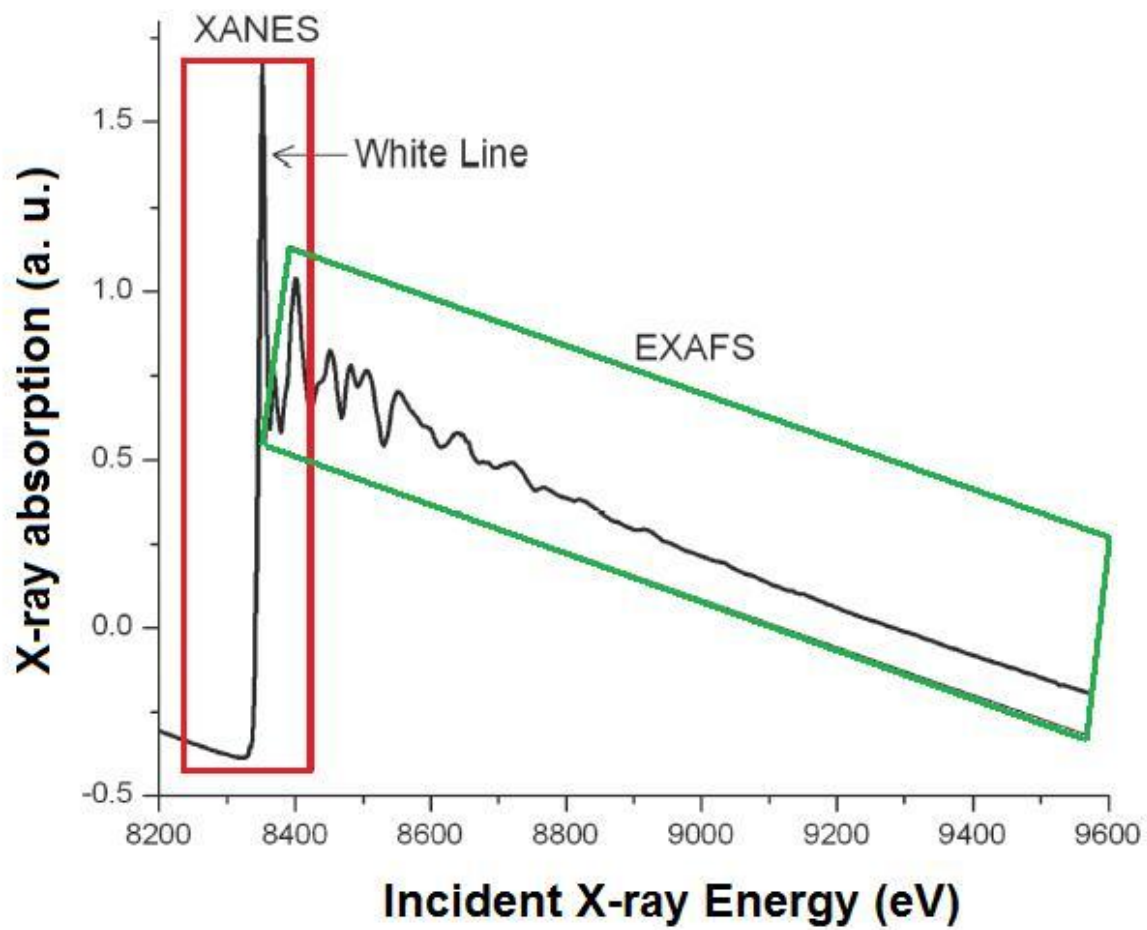


Figure 16. General XAS profile. [57]

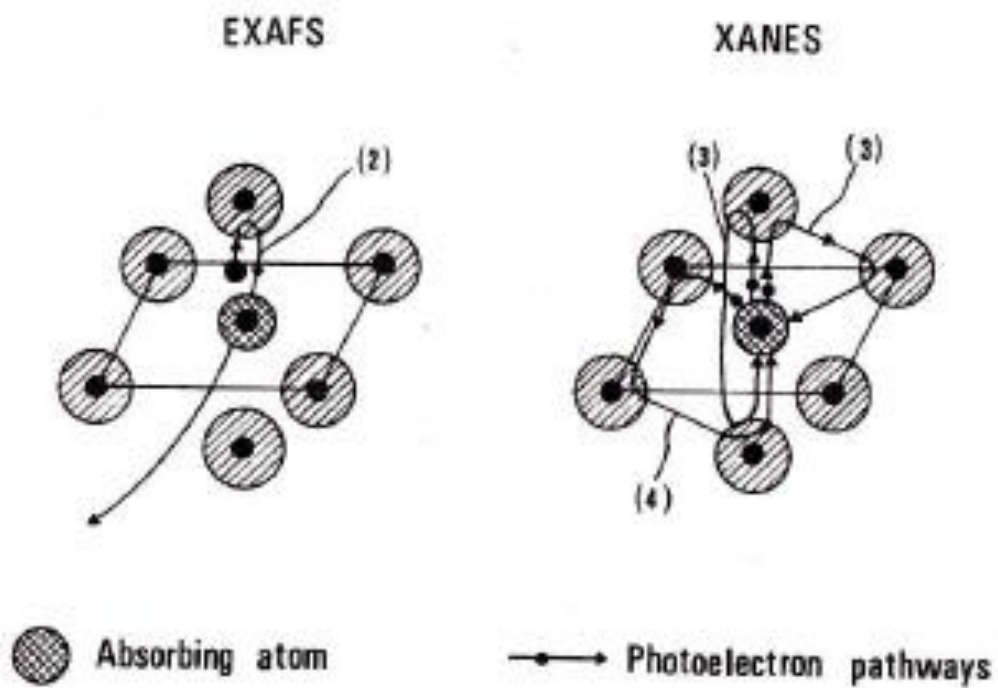


Figure 17. XAFS and XANES scattering pathways. [51]

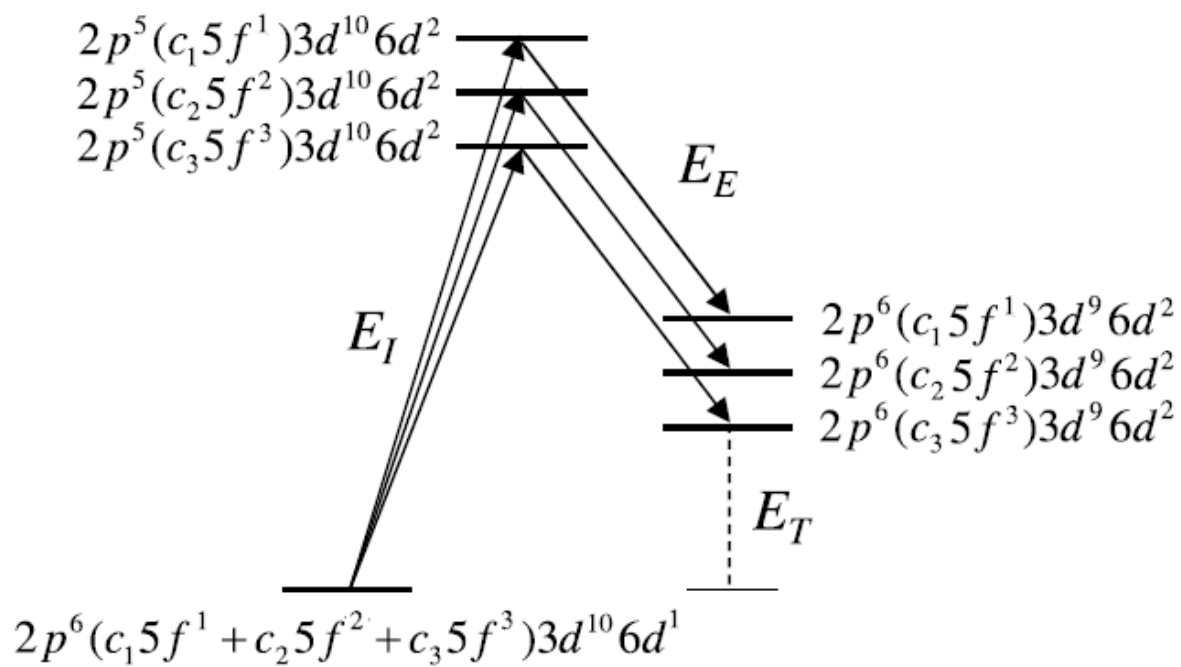


Figure 18. The fluorescence energy level diagram of the uranium L<sub>3</sub> edge. [11]



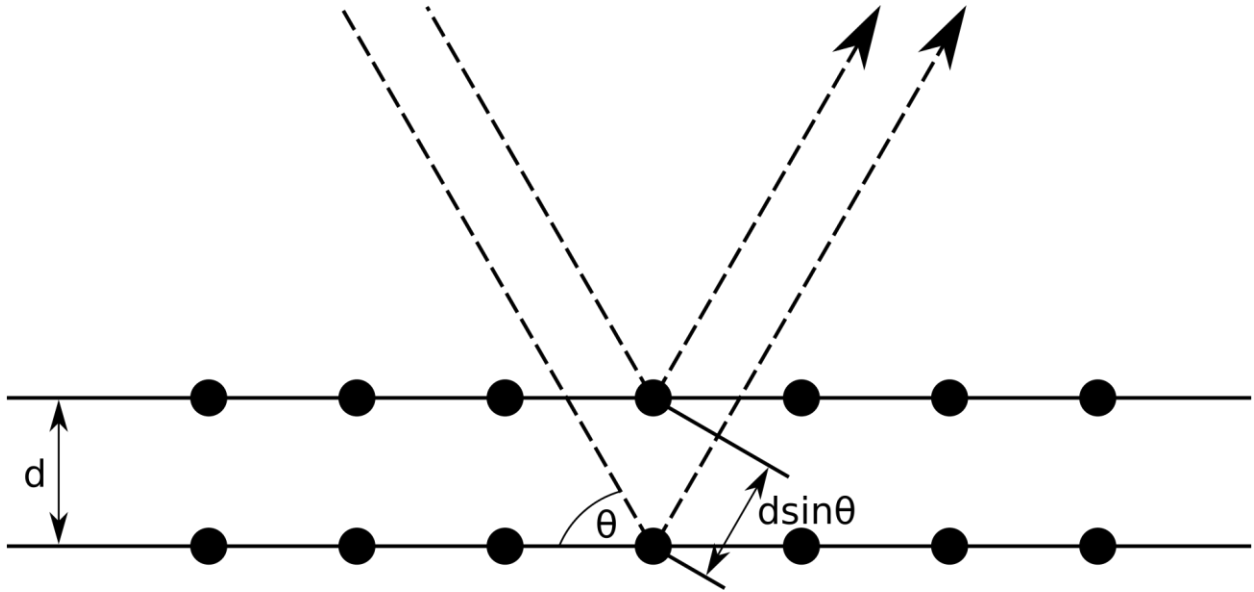
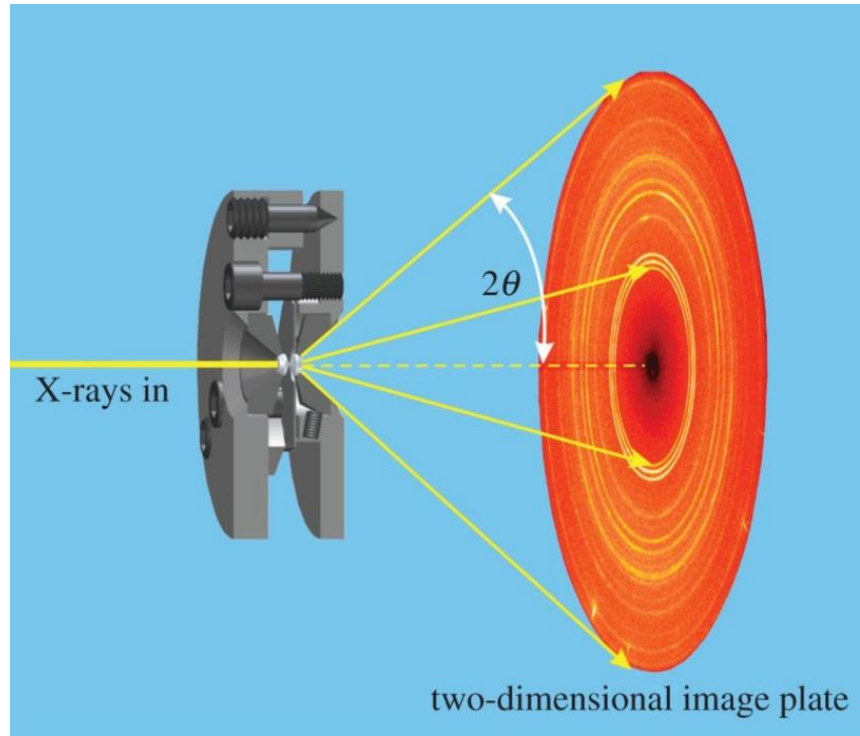
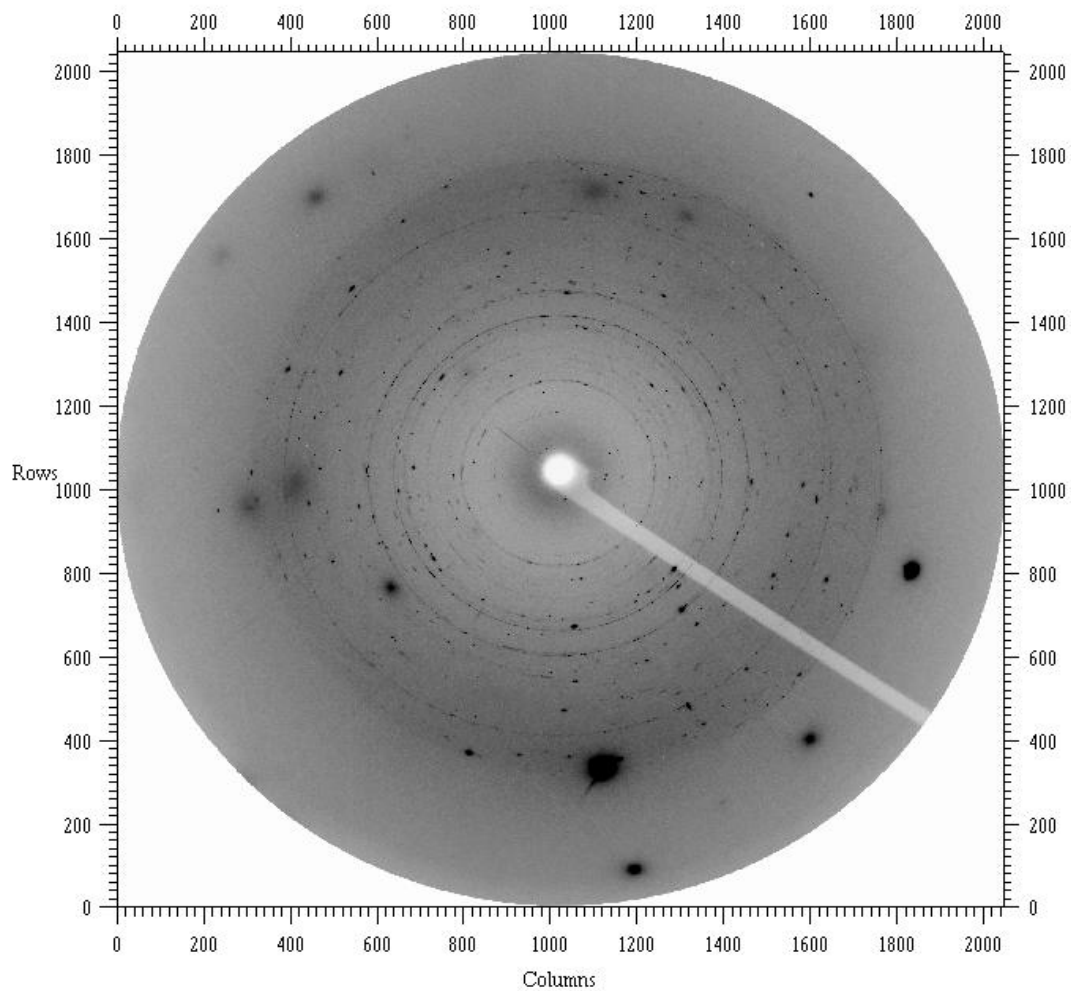


Figure 19. Bragg's Law. [66]



**Figure 20. High Pressure Powder Diffraction Geometry. [67]**



**Figure 21. An Example Raw Powder Diffraction Image.** Large dark spots are scattering off of large single crystals in the sample or the diamonds and are removed for powder analysis.

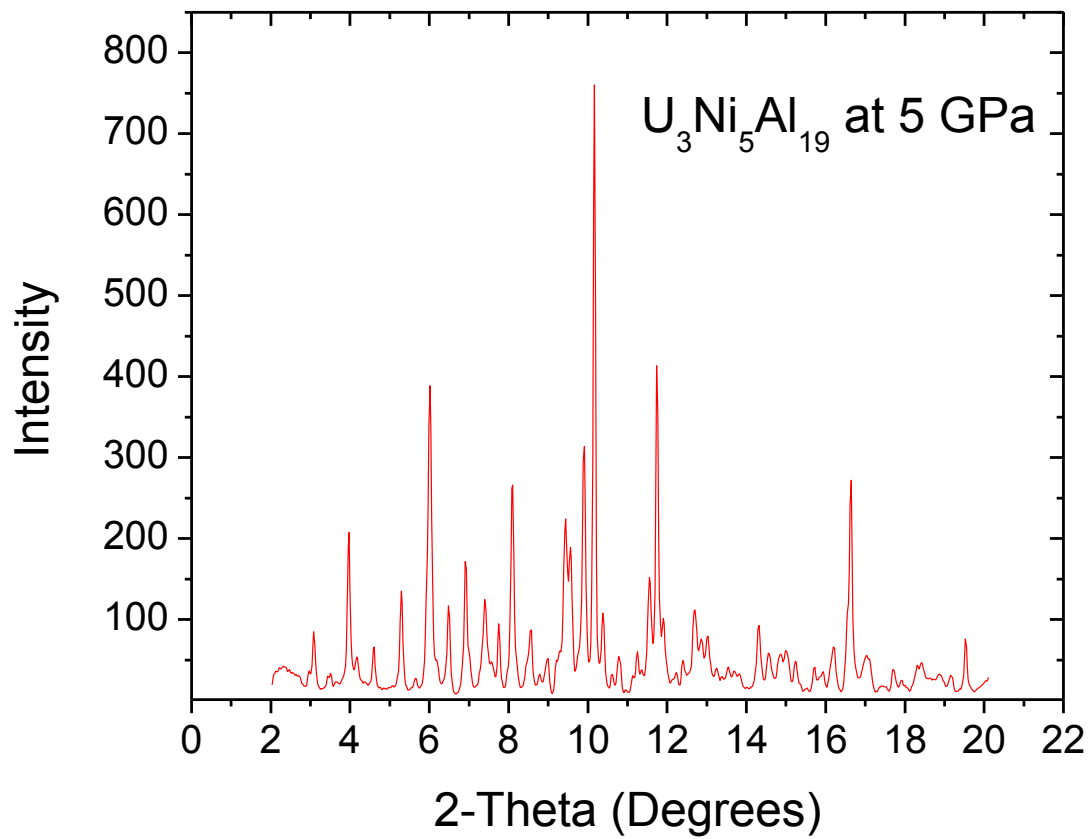


**Figure 22. An Example Integrated XRD Pattern.**

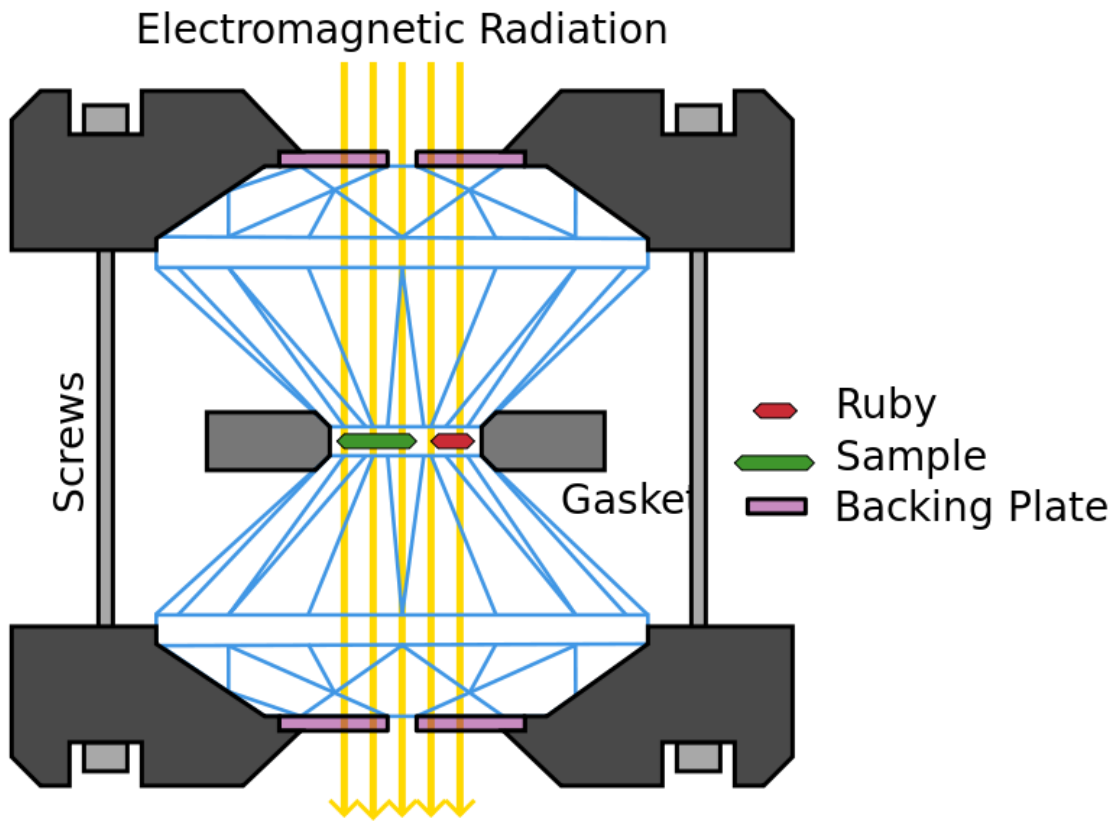


**Figure 23.** A Cutaway diagram of a typical diamond anvil cell. Not to Scale.

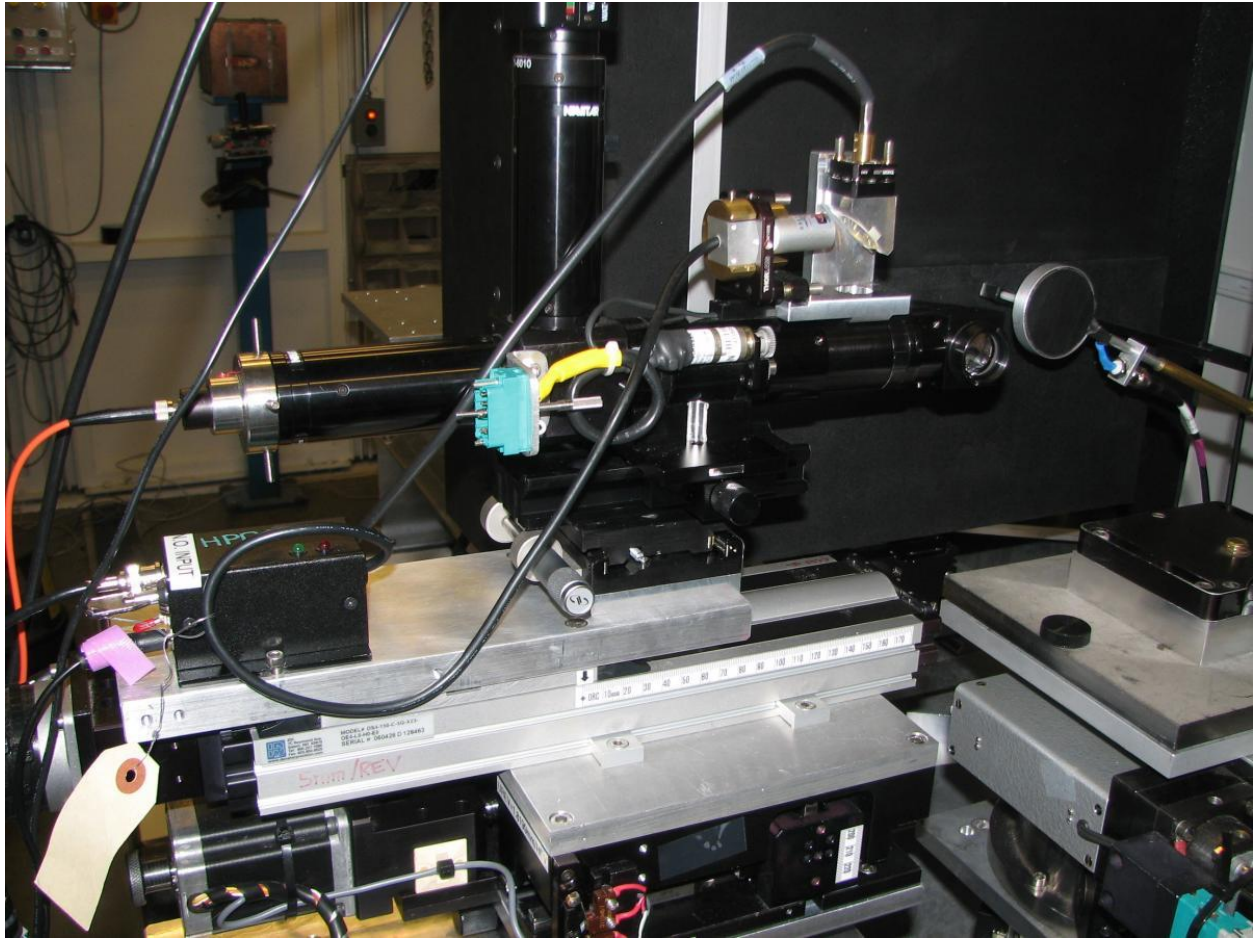


**Figure 24.** The online ruby spectrometer at HPCAT sector 16-IDB. It can remotely be moved in and out, allowing for pressure to be completely measured and changed from outside the experiment hutch.

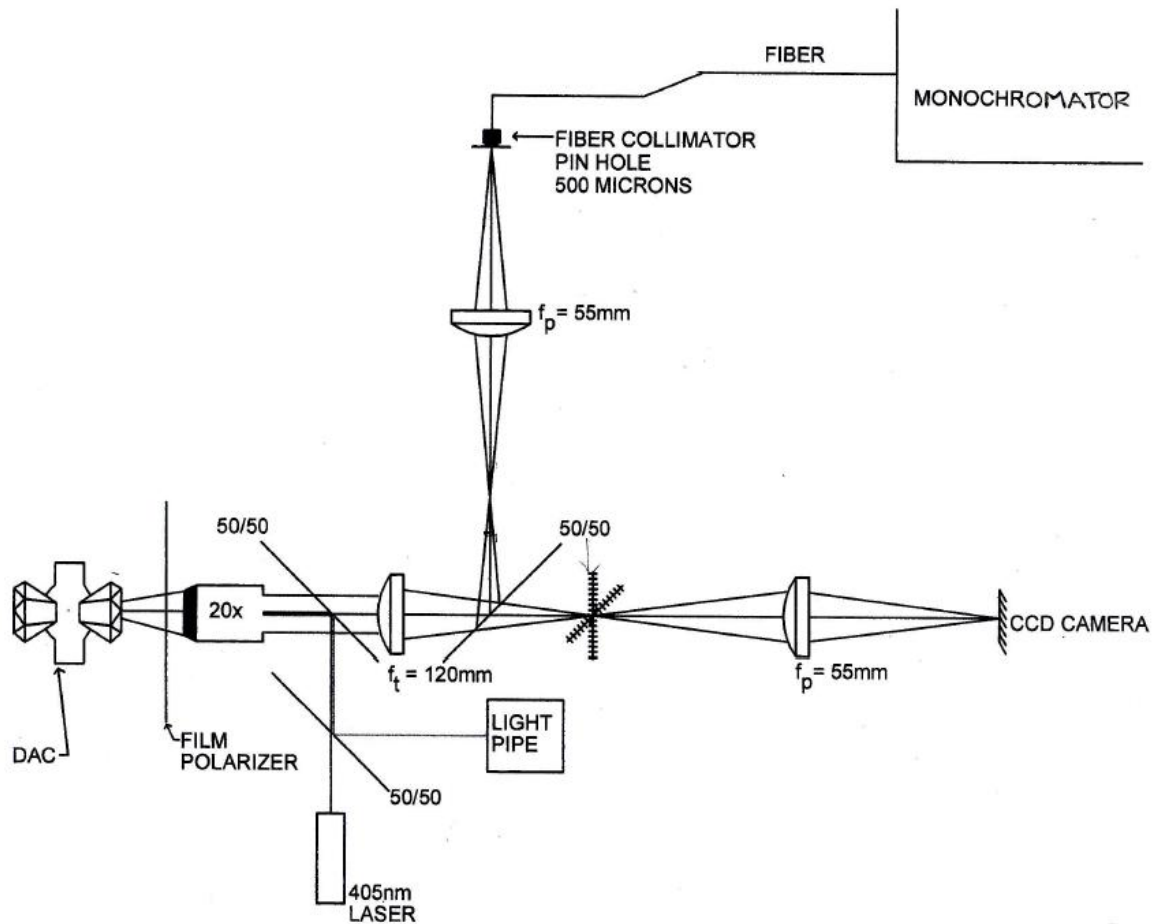
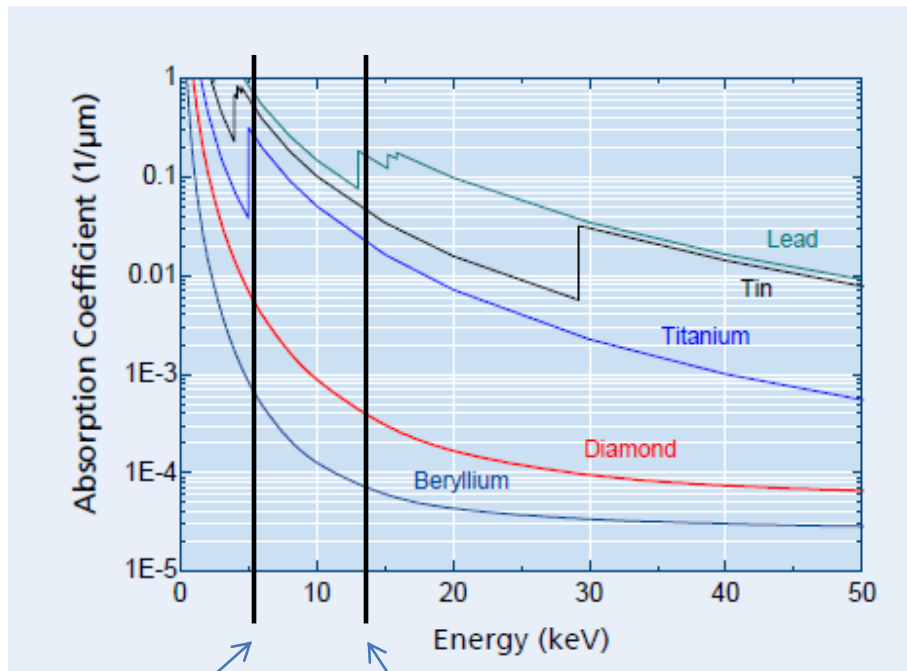


**Figure 25.** An example diagram of a ruby fluorescence detector. A CCD camera allows for aiming the laser and visual inspection of the sample as pressure is increased.



**Figure 26. Almax-Easylab CuBe non-magnetic Pressure cell.** Has a build-in gas membrane drive.





Ce L<sub>3</sub> ≈ 5.7 keV

U L<sub>3</sub> ≈ 13.2 keV

**Figure 27. The energy dependence of some absorption coefficients.** Diamond and Beryllium are relevant to these high pressure experiments.

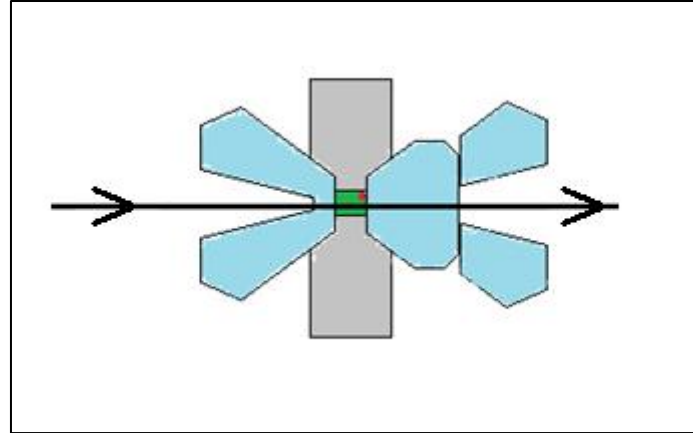


**Figure 28. Perforated diamond anvils.** This setup reduces the amount of diamond in the X-ray beam path, while still allowing optical access to the cell for pressure measurements.

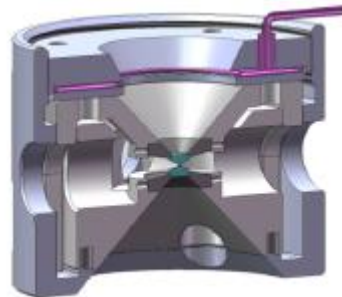


**Figure 29. A cutaway of a DAC with a gas membrane drive.** [80]

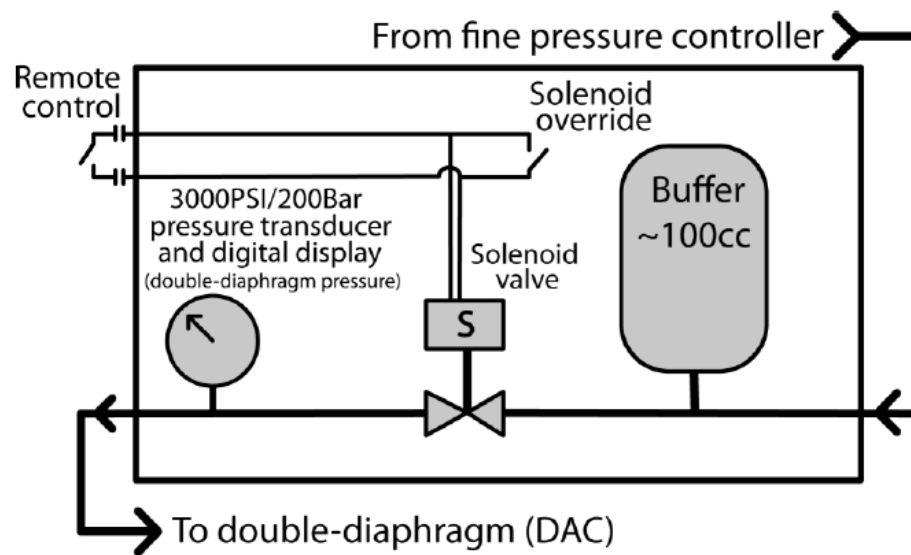


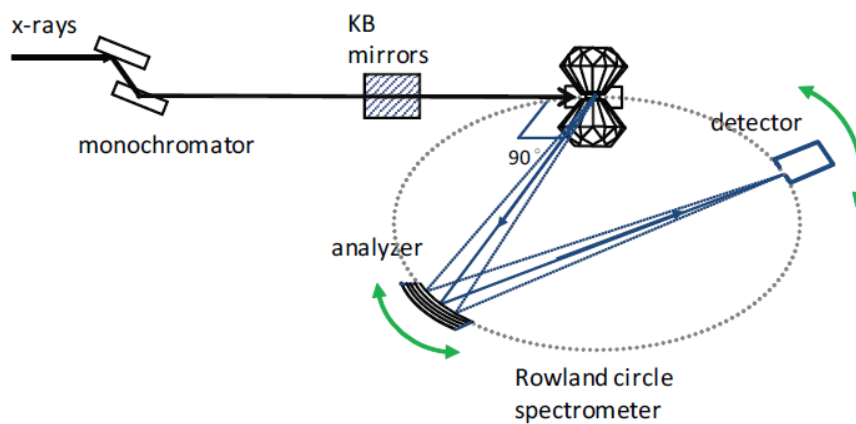
Figure 30. A diagram of a gas membrane pressure controller. [80]



Figure 31. A Paderborn-panoramic style DAC with beryllium gasket.



**Figure 32. A Princeton Mao-type symmetric cell.**



**Figure 33. The radial scattering geometry used in PFY acquisition.**



**Figure 34.** A four-posts wide-opening DAC. Designed for single crystal measurements.

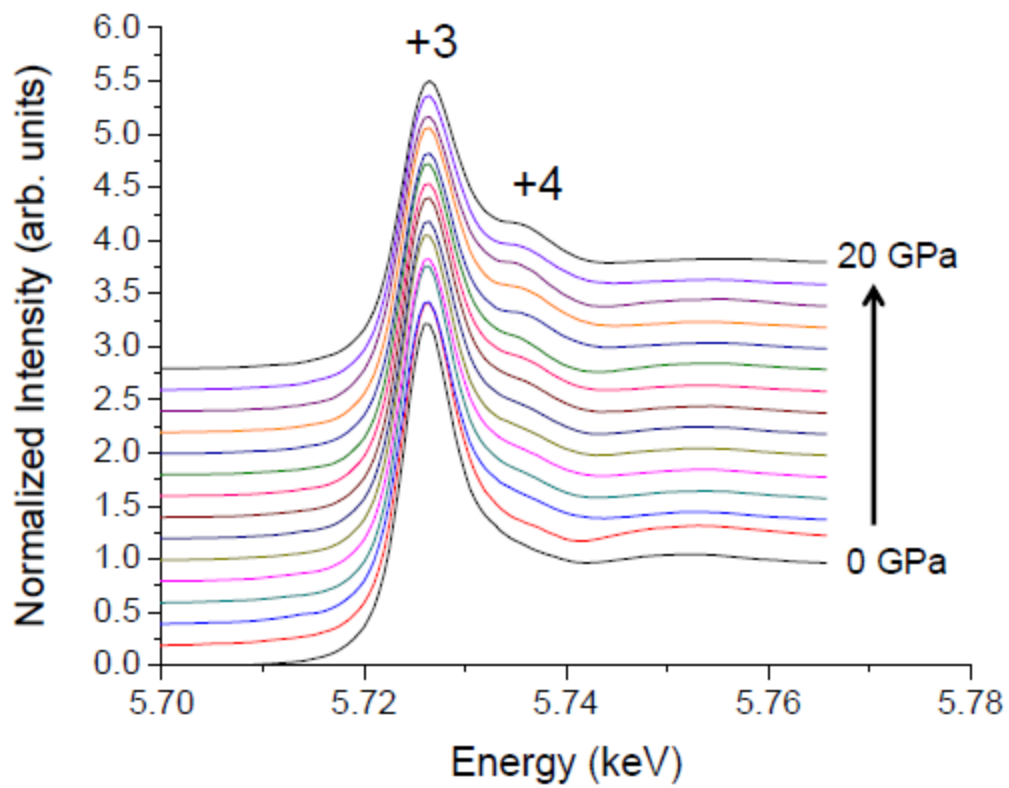


**Figure 35. The evolution of the  $CeCu_2Ge_2$   $L_3$  edge with Pressure at 10 K.**

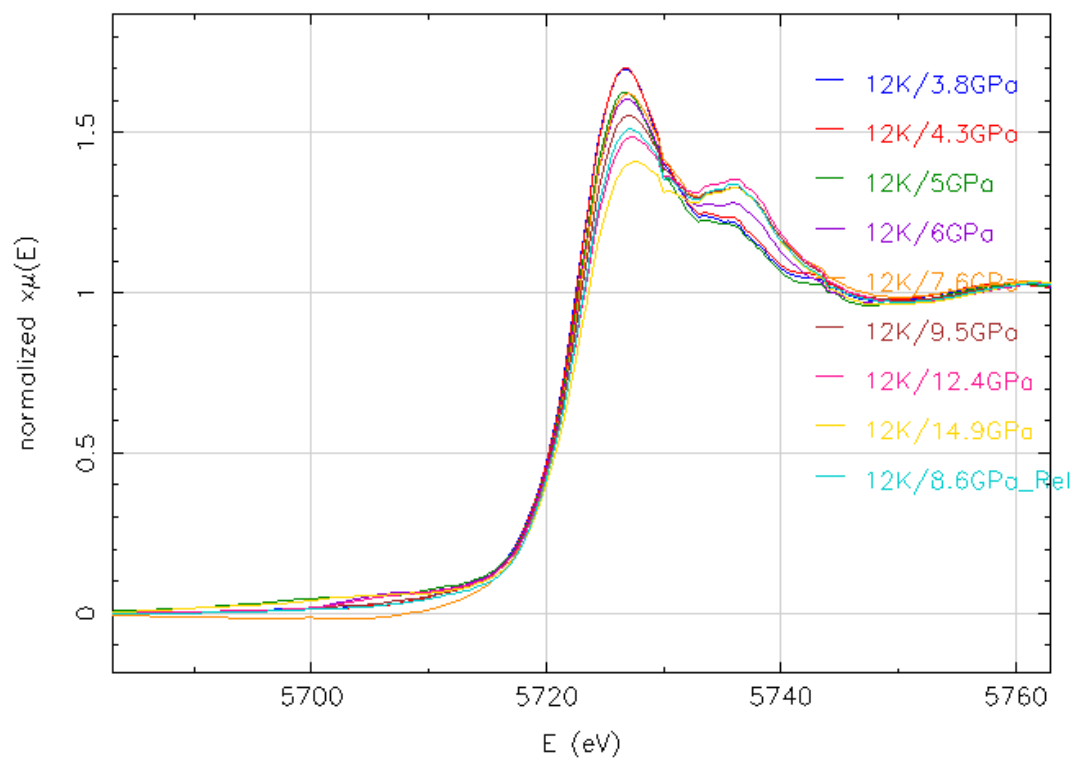


**Figure 36. The evolution of the CeCoSi  $L_3$  edge with pressure.** 12 Kelvin is the lowest temperature taken.

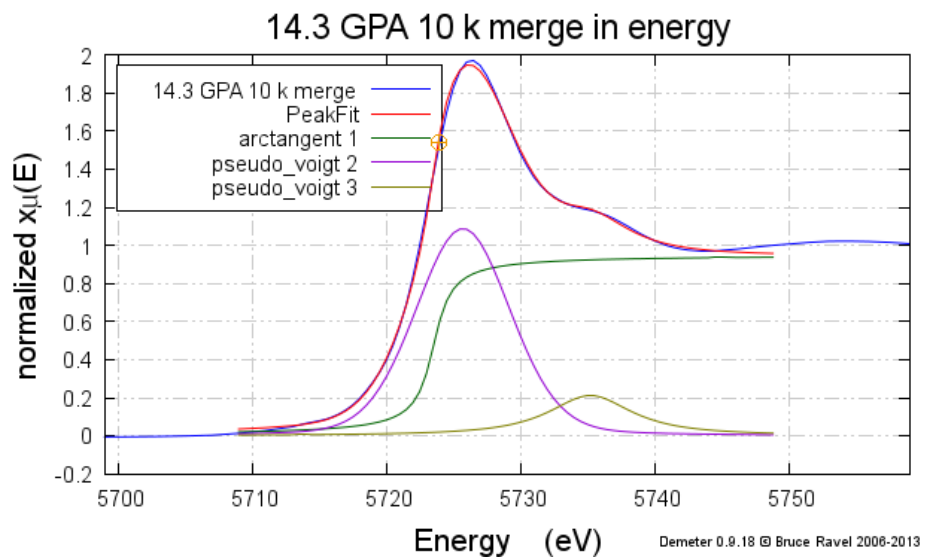


**Figure 37. Example of the fit to the intensity of the white line for  $\text{CeCu}_2\text{Ge}_2$ .**



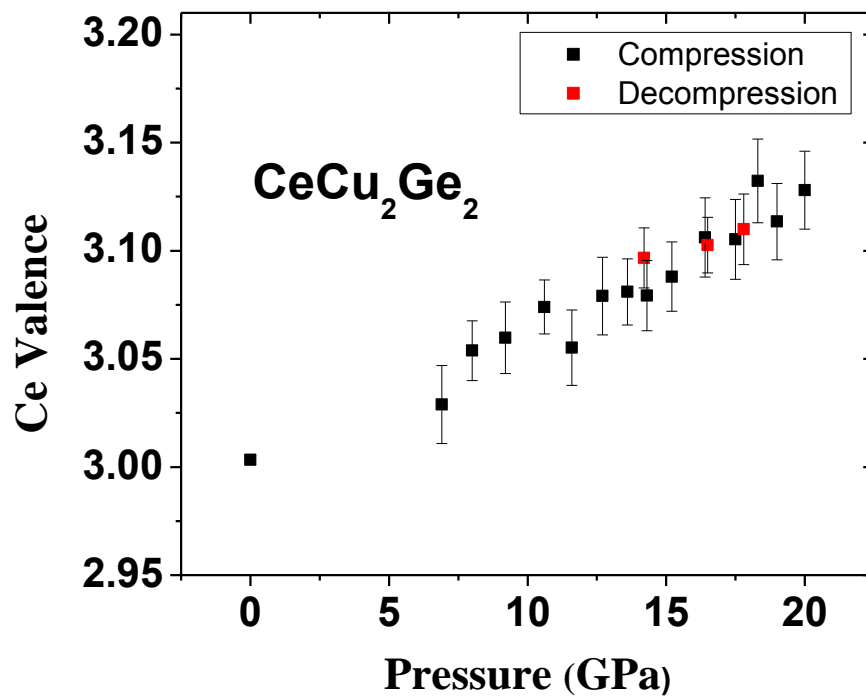


**Figure 38.** The change in Cerium Valence vs. Pressure of  $\text{CeCu}_2\text{Ge}_2$ . There is no valence discontinuity that would correspond to a volume collapse.

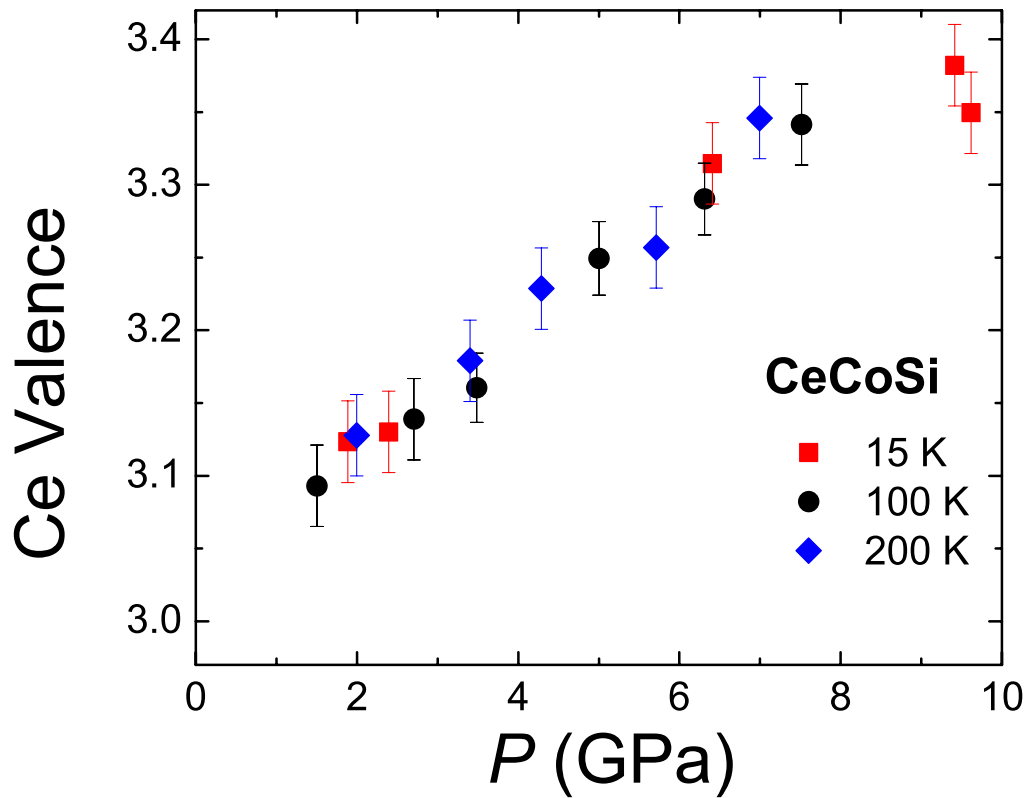


**Figure 39.** Ce valence from XANES data as a function of pressure for CeCoSi. Taken at different temperatures. There is no discernible valence discontinuity in the region of  $T_v$  shown in Fig. RR, but rather there is a typical smooth increase in valence at all three temperatures, which have very little temperature dependence.

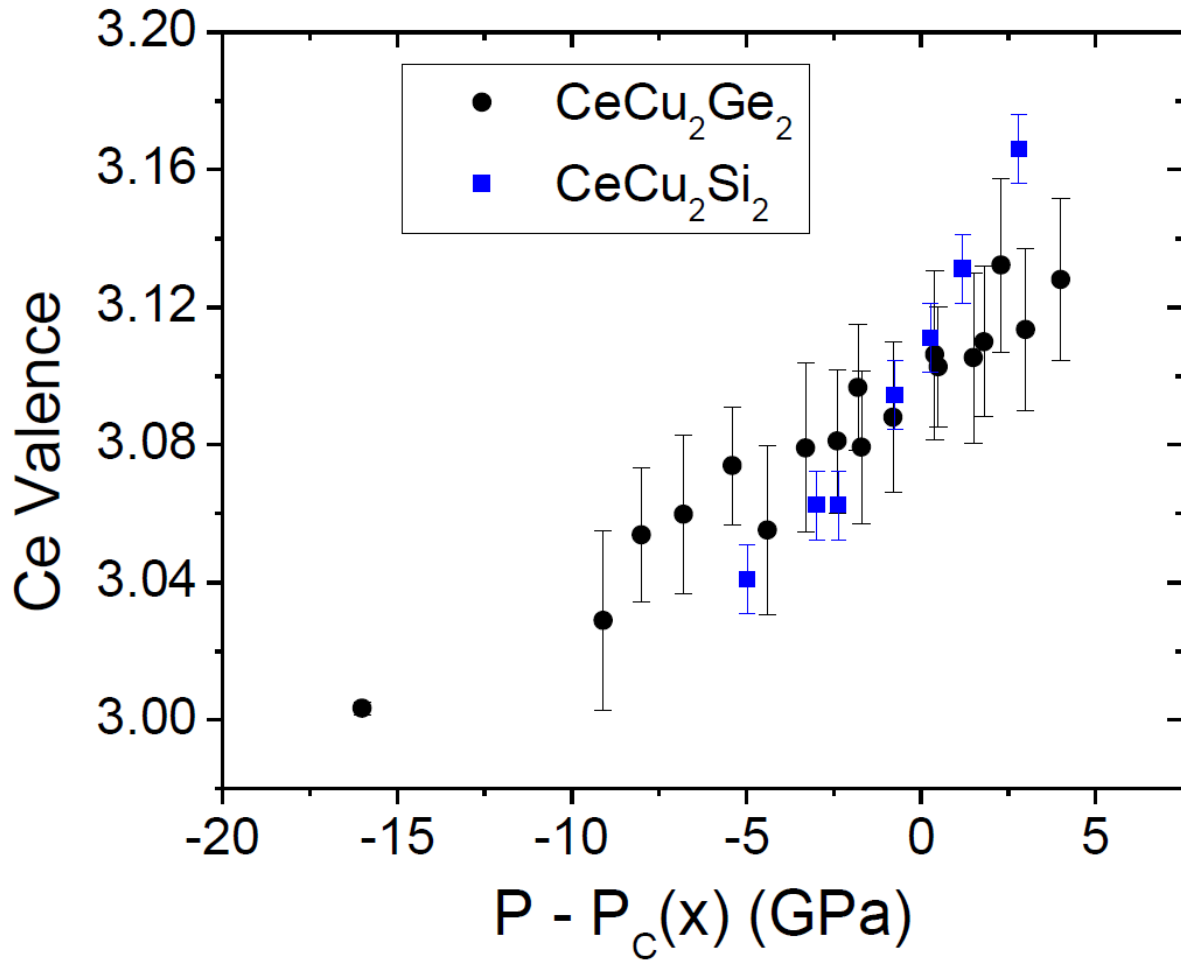


**Figure 40.** Comparison of Ce valence from CeCu<sub>2</sub>Ge<sub>2</sub> with CeCu<sub>2</sub>Si<sub>2</sub>. Pressure is scaled in relation to pressure at maximum superconducting transition temperature. The CeCu<sub>2</sub>Si<sub>2</sub> data is from Rueff *et al* [86].

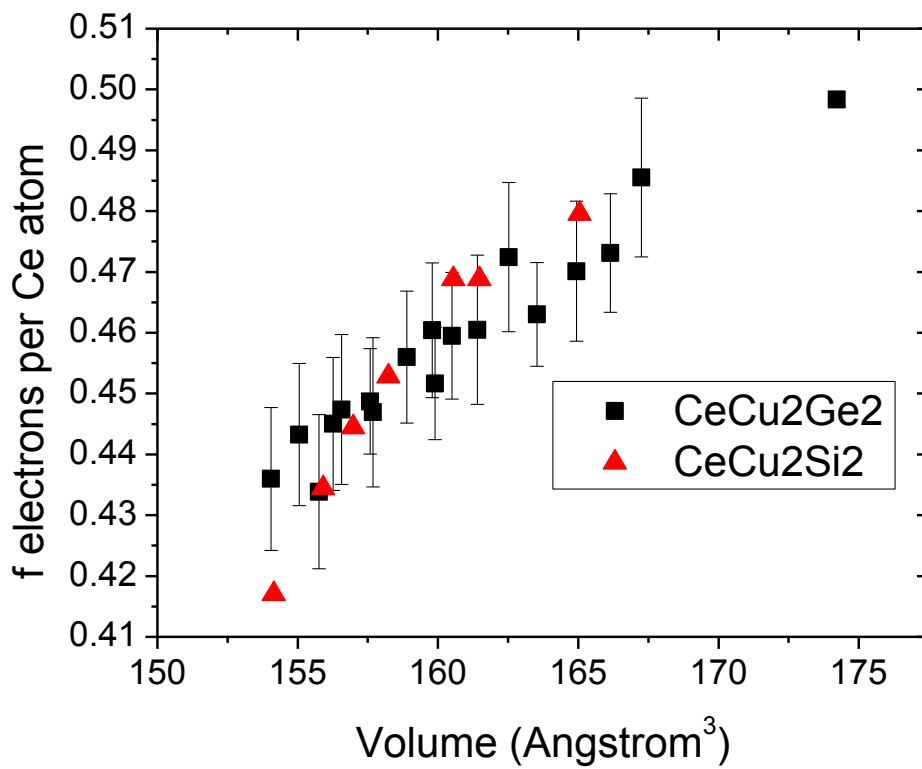
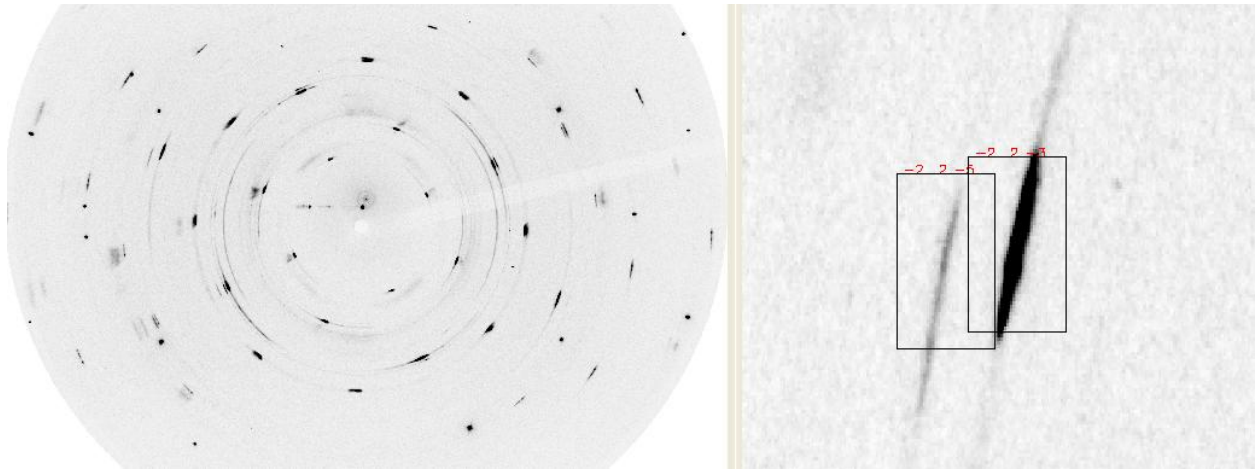
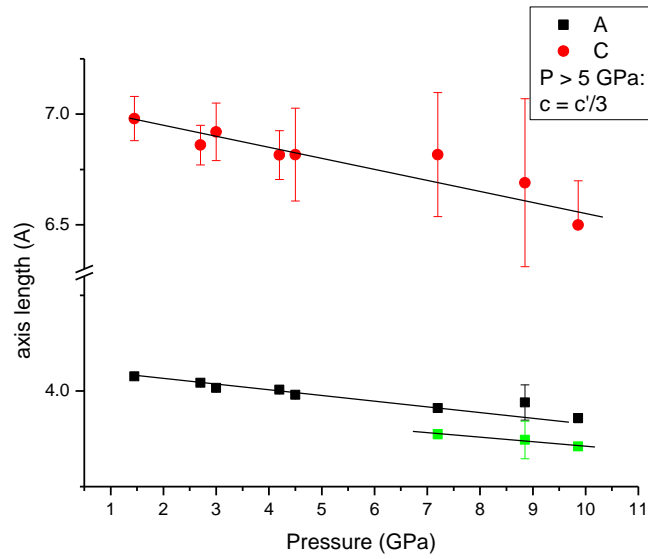


Figure 41. Conversion to f electron occupancy vs. unit cell volume [86].



**Figure 42. Single crystal XRD data of CeCoSi at 6 GPa.** Additional reflections ( $-2,0 -1$  shown) indicate a structural transition with a degree of disorder.



**Figure 43. The a, b, and c lattice parameters in CeCoSi as a function of pressure.** The C parameter is reduced by a factor of 3 above the phase transition at 5 GPa, forming a superlattice. A weak monoclinic/orthorhombic distortion along A is also seen.

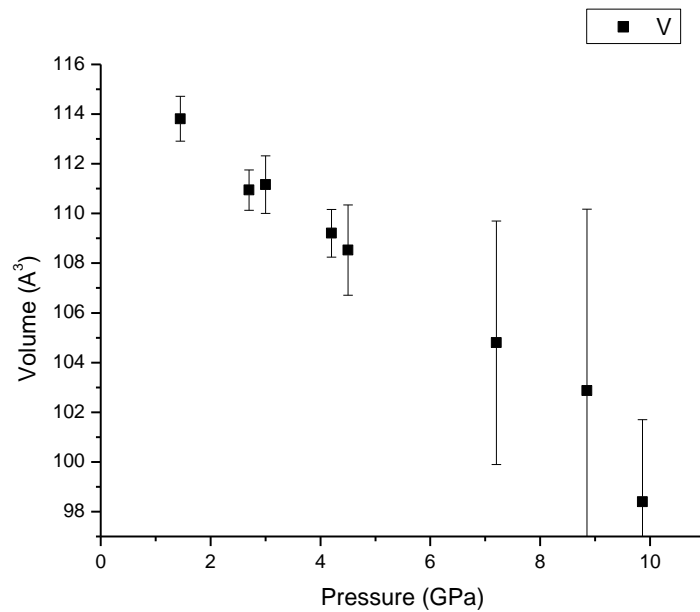


**Figure 44. Unit cell volume as a function of pressure of CeCoSi.** There appears to be no volume collapse after the 5 GPa transition, but experimental errors are large in the high pressure phase.

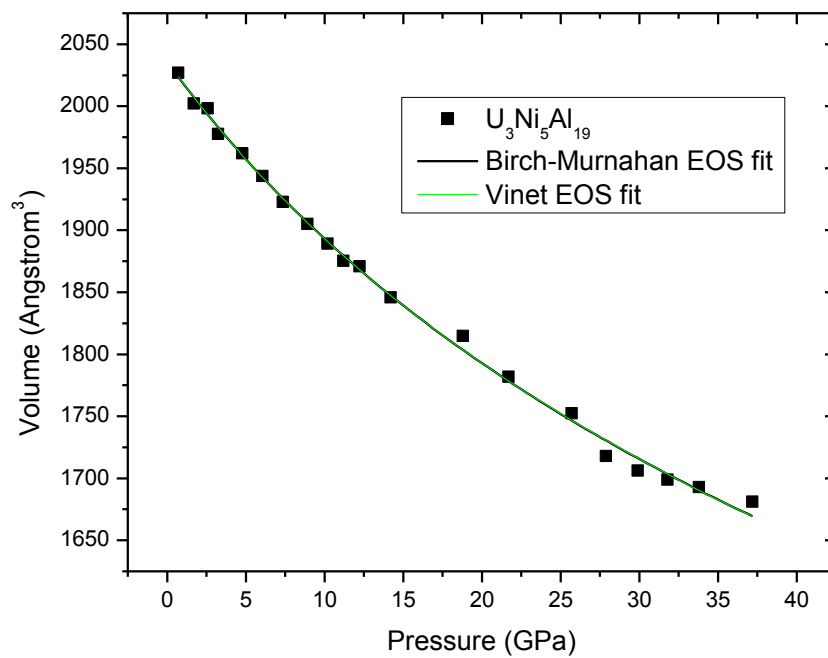


**Figure 45. Equation of state for U<sub>3</sub>Ni<sub>5</sub>Al<sub>19</sub>.**

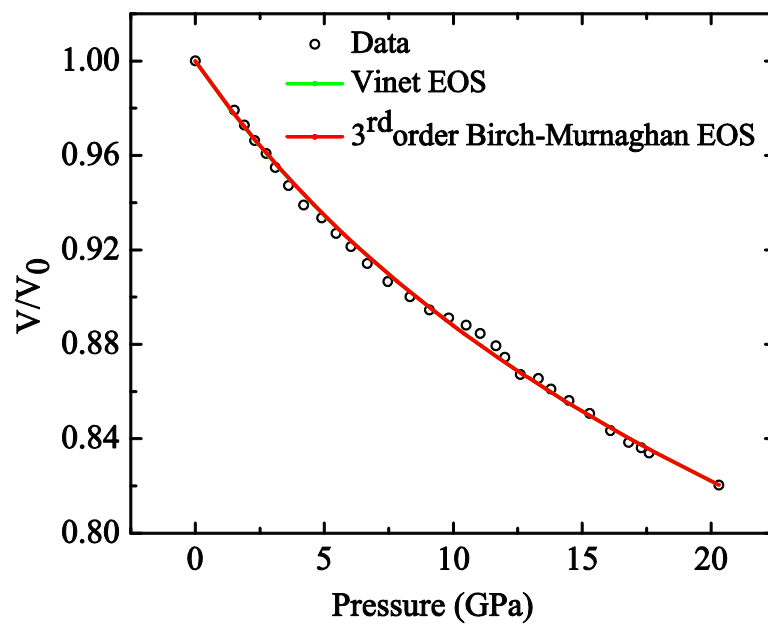
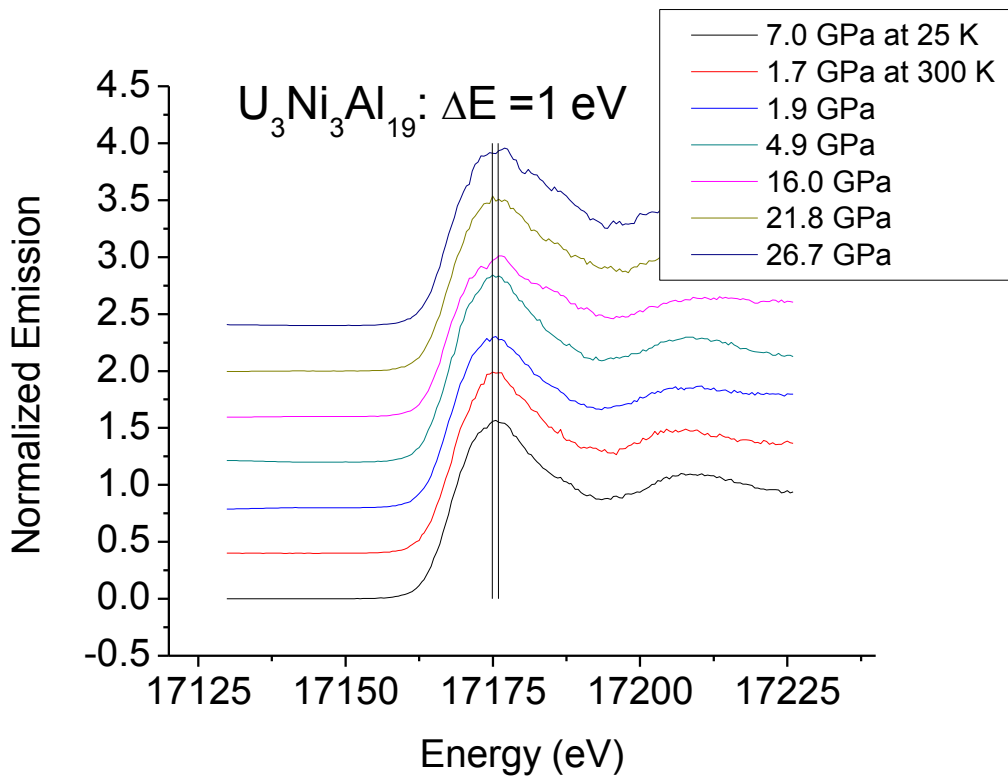
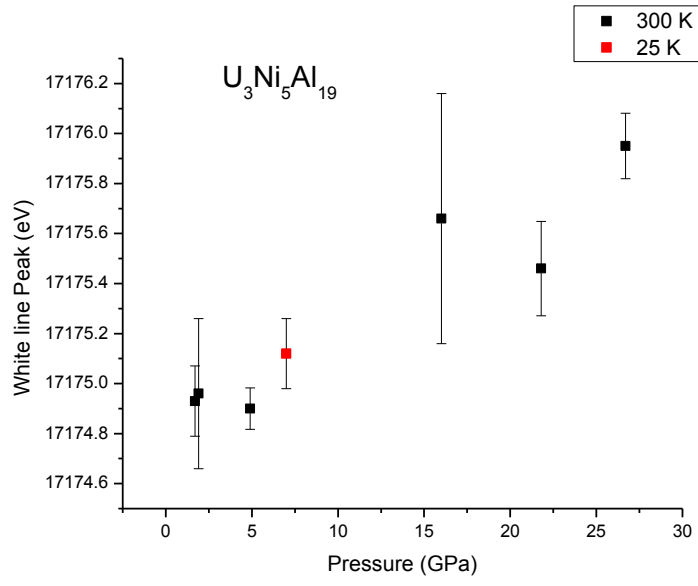


Figure 46. Equation of state for  $UCd_{11}$ .





**Figure 47. Evolution of the white line under pressure for  $U_3Ni_5Al_{19}$ . The position of the peak at highest and lowest pressure is shown by the vertical lines**



**Figure 48. The shift in the white line of  $U_3Ni_5Al_{19}$ .** The shift is fairly linear, and the single low temperature peak agrees with the room temperature data.

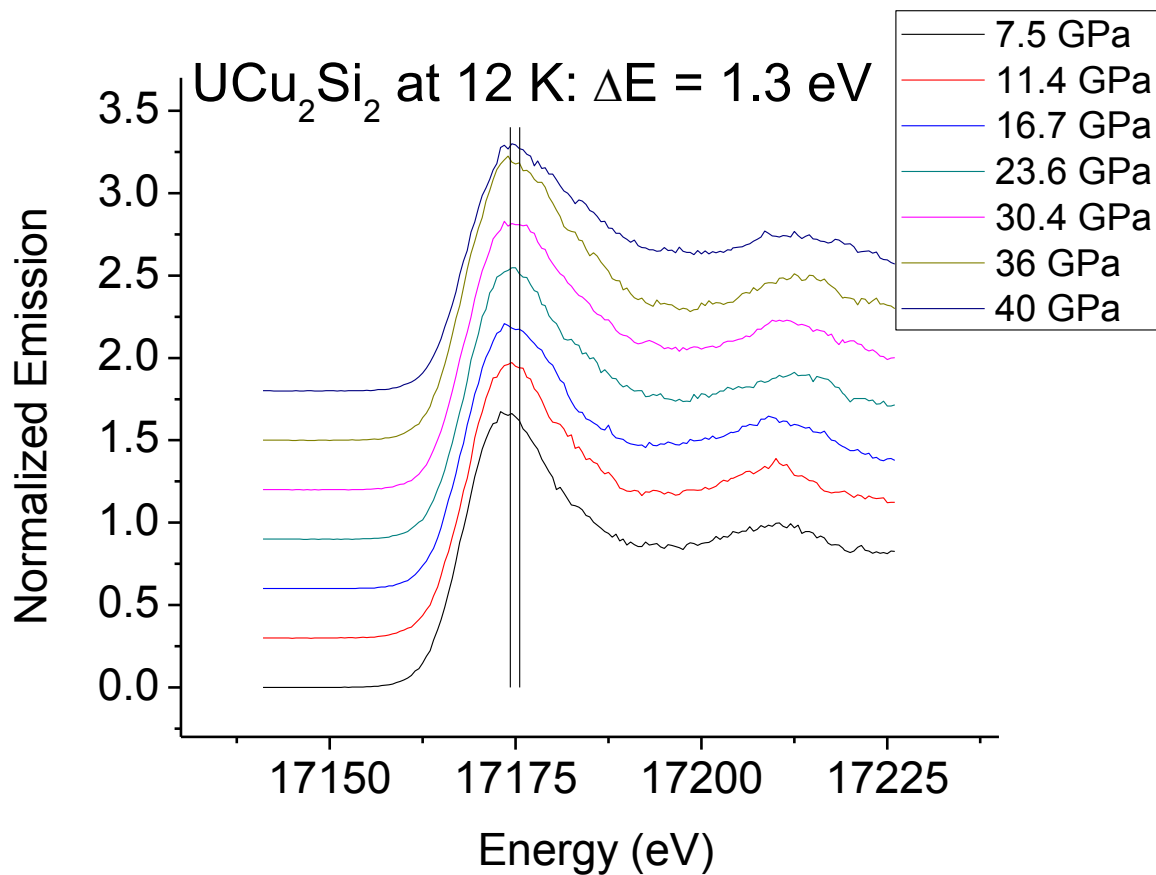


**Figure 49. Evolution of the white line under pressure for UCu<sub>2</sub>Si<sub>2</sub>.** The position of the peak at highest and lowest pressure is shown by the vertical lines.

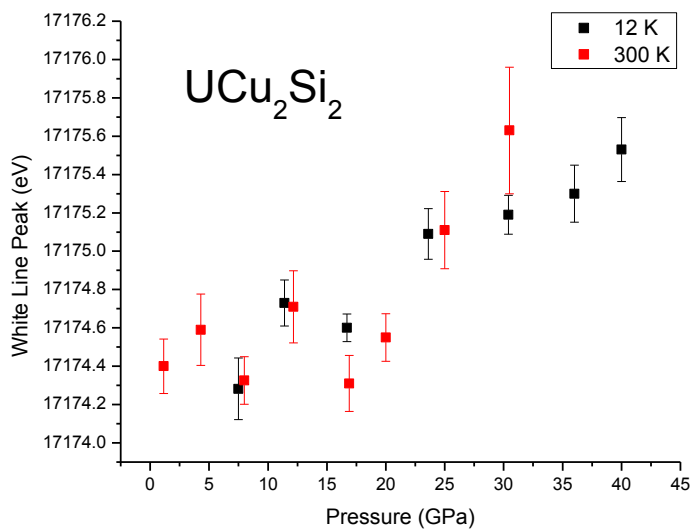


**Figure 50. The shift in the white line of  $UCu_2Si_2$ .** The shift is fairly linear, and the low temperature data agrees fairly well with the room temperature data.

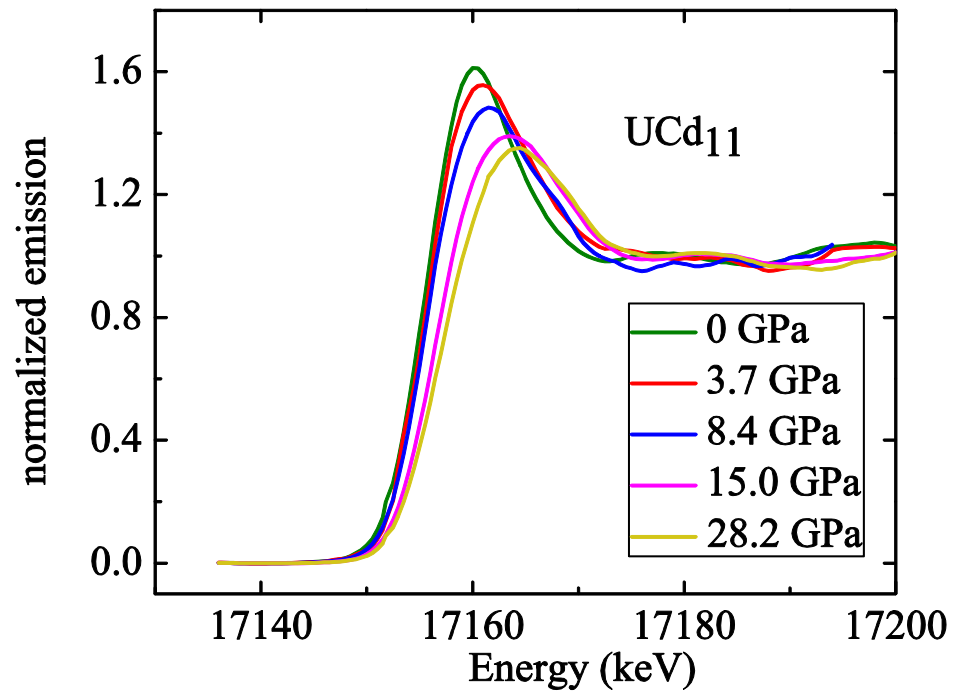


**Figure 51.** Evolution of the white line under pressure for UCd<sub>11</sub>. A noticeable shift in the composite peak is seen.

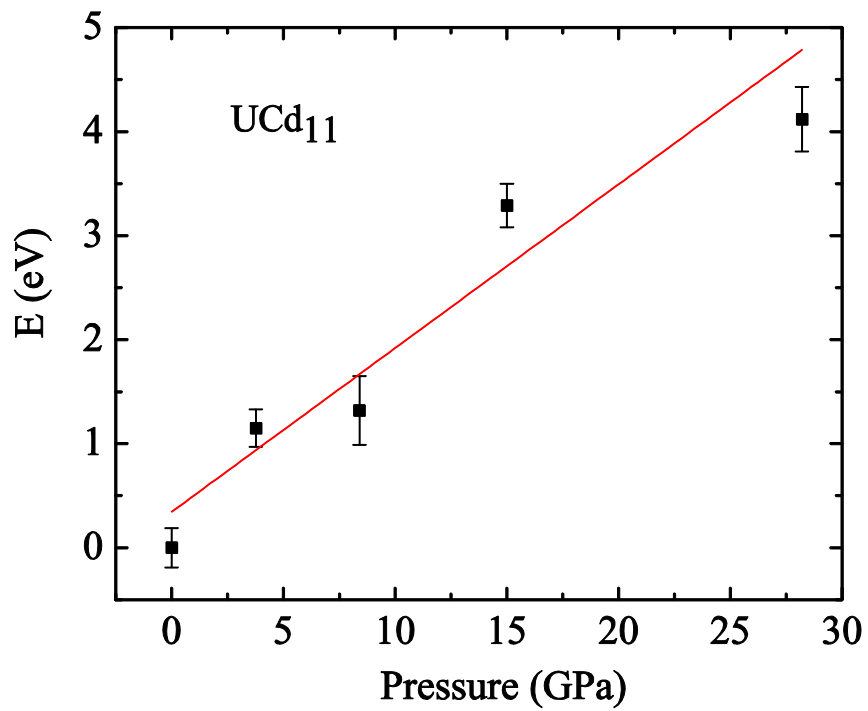


**Figure 52. Shift in White line peak from ambient pressure for UCd<sub>11</sub>.** A relatively large shift of 4.1 eV is seen, corresponding to roughly one less f electron occupancy at the uranium site.

## Appendix: Tables

**Table 1. Fit parameters for the EOS of UCd<sub>11</sub>.**

Type of equation of state	Bulk modulus (K <sub>0</sub> )	Bulk modulus derivative (K <sub>0</sub> ')
3 <sup>rd</sup> order Birch Murnaghan	62 ± 1.0	4.9 ± 0.2
Vinet	62 ± 1.0	5.2 ± 0.2

**Table 2. Fit parameters for the EOS of U<sub>3</sub>Ni<sub>5</sub>Al<sub>19</sub>.**

Type of equation of state	Bulk modulus (K <sub>0</sub> )	Bulk modulus derivative (K <sub>0</sub> ')
3 <sup>rd</sup> order Birch Murnaghan	115 ± 14.9	4.9 ± 1.1
Vinet	114 ± 15	5.1 ± 1.1

## References

- [1] C. Kittel *Introduction to Solid State Physics*. Wiley & Sons. (1953–1976).
- [2] J. Quintanilla and C. Hooley *The strong-correlations puzzle* *Physics World* **22**, No. 6, 32-37 (2009).
- [3] Hiroshi Maeda, Yoshiaki Tanaka, Masao Fukutomi and Toshihisa Asano, *Japanese Journal of Applied Physics, Part 2* **27**, L209, L210. (1988).
- [4] Masatoshi Imada, Atsushi Fujimori, and Yoshinori Tokura *Metal-insulator transitions* *Rev. Mod. Phys.* **70**, 1039 (1998).
- [5] Miron Y. Amusia, Konstantin G. Popov, Vasily R. Shaginyan, Vladimir A. Stephanovich *Theory of Heavy-Fermion Compounds: Theory of Strongly Correlated Fermi-Systems* Springer International Publishing Switzerland (2015) Chap. 1.
- [6] Miron Y. Amusia, Konstantin G. Popov, Vasily R. Shaginyan, Vladimir A. Stephanovich *Theory of Heavy-Fermion Compounds: Theory of Strongly Correlated Fermi-Systems* Springer International Publishing Switzerland (2015) Chap. 6.
- [7] A. L. Cornelius, A. J. Arko, J. L. Sarrao, and N. Harrison. *The haas-van alphen effect, magnetic transitions, and specific heat in the heavy-fermion system UCd<sub>11</sub>*. *Physical Review B*, **59(21)**, 13542-13545 (1999).
- [8] A. L. Cornelius, J. M. Lawrence, J. L. Sarrao, Z. Fisk, M. F. Hundley, G. H. Kwei, J. D. Thompson, C. H. Booth, and F. Bridges. *Experimental studies of the phase transition in YbIn<sub>1-x</sub>Ag<sub>x</sub>Cu<sub>4</sub>*. *Physical Review B* **56(13)**, 7993-8000, (1997).
- [9] J. C. Lashley, A. Lawson, R. J. McQueeney, and G. H. Lander *Absence of magnetic moments in plutonium* *Phys. Rev. B* **72**, 054416 (2005).
- [10] Y. S. Touloukian, E. H. Buyco, I. N. Lafayette *Thermophysical Properties of Matter - The TPRC Data Series. Volume 4. Specific Heat - Metallic Elements and Alloys* (1971)
- [11] C.H. Booth, Yu Jianga, D.L. Wangb, J.N. Mitchellc, P.H. Tobashc, E.D. Bauerd, M.A. Walle, P.G. Allene, D. Sokarasf, D. Nordlundf, T.C. Wengf, M.A. Torrezd, and J.L. Sarraog *Multiconfigurational nature of 5f orbitals in uranium and plutonium intermetallics* *PNAS* **109**, 26-10209 (2012).
- [12] N. W. Ashcroft, and N. D. Mermin, *Solid State Physics*, Philadelphia: Saunders College, pp 47 (1976).



- [13] N. E. Bickers, D. L. Cox, and J. W. Wilkins *Self-consistent large- $N$  expansion for normal-state properties of dilute magnetic alloys* Phys. Rev. B **36**, 2036 (1987).
- [14] Ashwani Kumar, P. K. Ahluwalia, S. Kumar, and K. C. Sharma *Competition between Kondo effect and RKKY interactions in heavy-fermion systems: Specific heat* Phys. Rev. B **56**, 3145 (1997).
- [15] S. Rahman, T. Mihalisin, J.E. Crow, P. Schlottmann *Competition between Kondo and RKKY interaction* Solid State Communications **75**, Issue 4, Pages 279–283 (1990).
- [16] M. J. Han, X. Wan, S.Y. Savrasov *Competition between Kondo and RKKY exchange couplings in  $Pu_{1-x}Am_x$  alloys* Phys. Rev. B **78**, 060401 (2008).
- [17] O. Stockert, J. Arndt, E. Faulhaber, C. Geibel, H. S. Jeevan, S. Kirchner, M. Loewenhaupt, K. Schmalzl, W. Schmidt, Q. Si, F. Steglich *Magnetically driven superconductivity in  $CeCu_2Si_2$*  Nature Physics **7**, 119–124 (2011).
- [18] Philipp Gegenwart, Qimiao Si, Frank Steglich *Quantum Criticality in Heavy Fermion Metals* Nature Physics **4**, 186 - 197 (2008).
- [19] Q. Si and S. Paschen *Quantum phase transitions in heavy fermion metals and Kondo insulators* Phys. Status Solidi B **250**, No. 3, 425–438 (2013).
- [20] Y. Tokiwa, J. J. Ishikawa, S. Nakatsuji, and P. Gegenwart *Quantum Criticality in a Metallic Spin Liquid System  $Pr_2Ir_2O_7$*  University of Tokyo Institute for Solid State Physics, Nakatsuji Group Activity Report (2013)
- [21] F. Steglich, J. Aarts, C. D. Bredl, W. Lieke, D. Meschede, W. Franz, and S. H., Phys. Rev. Lett. **43**, 1892 (1979).
- [22] M. J. Bull, K. A. McEwen, R. Osborn, R. S. Eccleston *Neutron intermultiplet spectroscopy of  $UPd_3$  and  $UPt_3$*  PHYSICA B-CONDENSED MATTER. 175 – 177 (1996).
- [23] E. L. Shirley, J. A. Soininen, J. J. Rehr *Modeling core-hole screening in core-excitation spectroscopies*. Phys Scr., **T115**, 31–34. (2005).
- [24] D. Jaccard, H. Wilhelm, K. Alami-Yadri, E. Vargoz *Magnetism and superconductivity in heavy fermion compounds at high pressure* Physica B **259-261**, 1-7 (1999).
- [25] Y. Kitaoka, H. Tou, G. Zheng, K. Ishida, K. Asayama, T.C. Kobayashi, A. Kohda, N. Takeshita, K. Amaya, Y. Onuki, G. Geibel, C. Schank, F. Steglich *NMR study of strongly correlated electron systems* Physica B **206 & 207**, 55-61 (1995).

- [26] H. Q. Yuan, M. Deppe, G. Sparn, F. M. Grosche, C. Geibel, and F. Steglich *PRESSURE EFFECT ON THE MAGNETISM AND SUPERCONDUCTIVITY IN SINGLE CRYSTAL CeCu<sub>2</sub>(Si<sub>0.9</sub>Ge<sub>0.1</sub>)<sub>2</sub>*. Acta Physica Polonica B, **34(2)**, 533-536. (2003).
- [27] H. Q. Yuan, F. M. Grosche, M. Deppe, C. Geibel, G. Sparn, F. Steglich *Observation of Two Distinct Superconducting Phases in CeCu<sub>2</sub>Si<sub>2</sub>* SCIENCE **302** (2003).
- [28] K. Miyake, O. Narikiyo, Y. Onishi *Superconductivity of Ce-based heavy fermions under pressure: Valence fluctuation mediated pairing associated with valence instability of Ce* Physica B **259-261**, 676-677 (1999).
- [29] Yoshifumi Onishi and Kazumasa Miyake *Enhanced Valence Fluctuations Caused by f-c Coulomb Interaction in Ce-Based Heavy Electrons: Possible Origin of Pressure-Induced Enhancement of Superconducting Transition Temperature in CeCu<sub>2</sub>Ge<sub>2</sub> and Related Compounds* Journal of the Physical Society of Japan **69**, No. 12, 3955-3964 (2000).
- [30] A. Onodera, S. Tsudukia, Y. Ohishib, T. Watanukic, K. Ishidaa, Y. Kitaokaa, Y. Onukid *Equation of state of CeCu<sub>2</sub>Ge<sub>2</sub> at cryogenic temperature* Solid State Communications **123**, 113–116 (2002).
- [31] T.C. Kobayashi, T. Miyazu, N. Takeshita, K. Shimizu, K. Amaya, Y. Kitaoka, Y. Onuki, J. Phys. Soc. Jpn **67**, 996 (1998).
- [32] Tatsuo C. Kobayashi, Kenji Fujiwara, Keiki Takeda, Hisatomo Harima, Yoichi Ikeda, Takafumi Adachi, Yasuo Ohishi, Christoph Geibel, Frank Steglich *Valence Crossover of Ce Ions in CeCu<sub>2</sub>Si<sub>2</sub> under High Pressure –Pressure Dependence of the Unit Cell Volume and the NQR Frequency* Journal of the Physical Society of Japan **82**, No. 11 (2013).
- [33] A. R. Denton and N. W. Ashcroft. *Vegard's law*. Phys. Rev. A **43**, (6) 3161–3164 (1991).
- [34] E. Lengyel, M. Nicklas, N. Caroca-Canales, and C. Geibel Physical Review B **88**, 155137 (2013).
- [35] R. Welter, G. Venturini, E. Ressouche, and B. Malaman Journal of Alloys and Compounds **210**, 279 (1994).
- [36] V. Iota, O. Tschauer, D. Haskel, D. Antonio, G. Fabris, E.D. Bauer, V. A. Sidorov, M. A. Torrez, F. Ronning, J. D. Thompson, C.H. Booth, Yusheng Zhao, and A.L. Cornelius *Interplay between structure, valence and superconductivity in Heavy Fermion Compound CeCoSi*, to be published.
- [37] B. Chevalier, S. F. Matar, J. S. Marcos, and J. R. Fernandez, Physica B-Condensed Matter **378-380**, 795 (2006).
- [38] Z. Fisk, G. R. Stewart, J. O. Willis, H. R. Ott, and F. Hulliger, Phys. Rev. B **30**, 6360 (1984).

- [39] H. H. Hill, *The 'early' actinides; The Periodic System's f electron transition metal series*, in *Plutonium and Other Actinides*, edited by W.N. Miner, (AIME, New York) (1970).
- [40] J. D. Thompson, A. C. Lawson, M. W. McElfresh, A. P. Sattelberger, and Z. Fisk *J. Magn. Magn. Mater.* **76-77**, 437 (1988).
- [41] C. R. Andraka, B. Andraka, G. R. Stewart, Y. Takano and Z. Fisk, *J. Appl. Phys* **97**, 10A912 (2005).
- [42] E. Yamamoto, Y. Hirose, K. Enoki, K. Mitamura, K. Sugiyama, T. Takeuchi, M. Hagiwara, K. Kindo, Y. Haga, R. Settai, and Y. Onuki *J. Phys. Soc. Jpn.* **81**, SB023 (2012).
- [43] B. Andraka, G. R. Stewart, and Z. Fisk, *Phys. Rev. B* **44**, 10346 (1991).
- [44] R. E. Gladshetskii, K. Cenxual, and E. Parthé, *J. Solid State Chem.* **100**, 9 (1992).
- [45] E. D. Bauer, V. A. Sidorov, S. Bobev, I. D. J. Mixson, J. D. Thompson, J. L. Sarrao, and M. F. Hundley *High-pressure investigation of the heavy-fermion antiferromagnet  $U_3Ni_5Al_{19}$*  Physical review. B, Condensed matter **71** 1 (2005).
- [46] R. Troć, M. Samsel-Czekala, J. Stępień-Damm, and B. Coqblin *Interplay between ferromagnetism, SDW order, and underscreened Kondo lattice in  $UCu_2Si_2$*  PHYSICAL REVIEW B **85**, 224434 (2012).
- [47] Z. Fisk, N. O. Moreno and J. D. Thompson *Properties of Cu-flux-grown  $UCu_2Si_2$*  *J. Phys.: Condens. Matter* **15** S1917–S1921 (2003).
- [48] M. Kuznietz, *J. Phys.: Condens. Matter* **15** 8957 (2003).
- [49] Z. Fisk, *et al.* *J. Phys.: Condens. Matter* **15** 8967 (2003).
- [50] A.L. Cornelius, R.S. Kumara, M.K. Jacobsena, E.D. Bauerb, J.S. Sarraob, Z. Fisk *Magnetic ordering in  $UCu_2Si_2$  at high pressure* *Physica B* **403** 940–942 (2008).
- [51] D. C. Koningsberger and R. Prins *X-ray Absorption: Principles, Applications, Techniques of EXAFS, SEXAFS, and XANES*. New York: Wiley & Sons pg 577-578 (1988).
- [52] D. C. Koningsberger and R. Prins *X-ray Absorption: Principles, Applications, Techniques of EXAFS, SEXAFS, and XANES*. New York: Wiley & Sons pg 53 (1988).
- [53] D. C. Koningsberger and R. Prins *X-ray Absorption: Principles, Applications, Techniques of EXAFS, SEXAFS, and XANES*. New York: Wiley & Sons pg 618-624 (1988).
- [54] Antonio Bianconi *Surface X-Ray Absorption Spectroscopy: Surface EXAFS and Surface XANES*. Applications of Surface Science **6**, 392-418 (1980).

- [55] Annibale Mottana and Marcelli Augusto *The historical development of X-ray Absorption Fine Spectroscopy and of its applications to Materials Science*. Physics, Astronomy and Engineering. A Bridge between Conceptual Frameworks and Technologies Springer Book Series: History of Mechanism and Machine. Netherlands: Springer (2013).
- [56] "X-ray absorption spectroscopy." *Wikipedia: The Free Encyclopedia*. Wikimedia Foundation, Inc. 15 May 2009. Web. 5 Nov. 2015.
- [57] Adapted from S. D. Kelly, D. Hesterberg, and B. Ravel in *Methods of Soil Analysis: Part 5, Mineralogical Methods*, Ed. A. L. Urely and R. Drees, Soil Science Society of America Book Series, Madison (2008).
- [58] W. Kossel, *Z. Phys.* **1**, 119 (1920).
- [59] R. de L. Kronig, *Z. Phys.* **70**, 317 (1931).
- [60] Boon K. Teo *EXAFS: Basic Principles and Data Analysis*, Springer Berlin Heidelberg (1986).
- [61] J. C. Fuggle and J. E. Inglesfield Eds. *Topics in Applied Physics: Unoccupied Electronic States: Fundamentals for XANES, EELS, IPS, and BIS*, Springer-Verlag (1992).
- [62] Isabella Ascone *X-ray Absorption Spectroscopy for Beginners* Talk: Chimie ParisTech, UMR C.N.R.S. 7223 (2011).
- [63] G. Bunker *Introduction to XAFS: A practical guide to X-ray Absorption Fine Structure Spectroscopy*, Cambridge University Press pg 137 (2010).
- [64] E. A. Stern and K. Kim *Thickness effect on the extended-x-ray-absorption-fine-structure amplitude* *Phys. Rev. B* **23**, 3781 (1981).
- [65] G. Bunker *Introduction to XAFS: A practical guide to X-ray Absorption Fine Structure Spectroscopy*, Cambridge University Press pg 91 (2010).
- [66] "Bragg's law." *Wikipedia: The Free Encyclopedia*. Wikimedia Foundation, Inc. 10 April 2009. Web. 5 Nov. 2015
- [67] M. I. McMahon *Diamonds on Diamond: structural studies at extreme conditions on the Diamond Light Source*, *Phil. Trans. R. Soc. A* **373**, 20130158 (2015).
- [68] A. P. Hammersley *FIT2D: An Introduction and Overview* ESRF Internal Report, **ESRF97HA02T** (1997).
- [69] A. P. Hammersley, S. O. Svensson, M. Hanfland, A. N. Fitch, and D. Häusermann, *Two-Dimensional Detector Software: From Real Detector to Idealised Image or Two-Theta Scan*, *High Pressure Research* **14**, 235-248 (1996).

- [70] Francis Birch *Finite Elastic Strain of Cubic Crystals*, Phys. Rev. **71**, 809 (1947).
- [71] Pascal Vinet, John R. Smith, John Ferrante, and James H. Rose *Temperature effects on the universal equation of state of solids*, Phys. Rev. B **35** (1945) – Published 1987.
- [72] L. Dubrovinsky, N. Dubrovinskaia, E. Bykova, M. Bykov, V. Prakapenka, C. Prescher, K. Glazyrin, H.-P. Liermann, M. Hanfland, M. Ekholm, Q. Feng, L. V. Pourovskii, M. I. Katsnelson, J. M. Wills, and I. A. Abrikosov *The most incompressible metal osmium at static pressures above 750 GPa*; Nature (2015).
- [73] "Diamond Anvil Cell." *Wikipedia: The Free Encyclopedia*. Wikimedia Foundation, Inc. 12 May 2012. Web. 5 Nov. 2015
- [74] A. Jayaraman, *Diamond anvil cell and high-pressure physical investigations* Rev. Mod. Phys. **55**, 65 (1983)
- [75] S. Klotz, J. C. Chervin, P. Munsch, and G. Le Marchand *Hydrostatic limits of 11 pressure transmitting media* J. Phys. D: Appl. Phys. **42**, 075413 (2009).
- [76] Mark Rivers, Vitali B. Prakapenka, Atsushi Kubo, Clayton Pullins, Christopher M. Holl, Steven D. Jacobsen, *The COMPRES/GSECARS gas-loading system for diamond anvil cells at the Advanced Photon Source*, High Pressure Res. **28** (3), 273-292 (2008).
- [77] A. D. Chijioke, W. J. Nellis, A. Soldatov, and I. F. Silvera *The ruby pressure standard to 150 GPa*, J. Appl. Phys. **98**, 114905 (2005).
- [78] H. K. Mao, J. Xu, and P. M. Bell, *J. Calibration of the Ruby Pressure Gauge to 800 kbar Under Quasi-Hydrostatic Conditions*. Geophys. Res. **91**, 4673 (1986).
- [79] P. C. Canfield and Z. Fisk *Growth of single crystals from metallic fluxes*, Philos Mag B **65**, 1117–1123 (1992).
- [80] Stanislav V. Sinogeikin, Jesse S. Smith, Eric Rod, Chuanlong Lin, Curtis Kenney-Benson, and Guoyin Shen *Online remote control systems for static and dynamic compression and decompression using diamond anvil cells* REVIEW OF SCIENTIFIC INSTRUMENTS **86**, 072209 (2015).
- [81] P. Dera, K. Zhuravlev, V. Prakapenka, M. L. Rivers, G. J. Finkelstein, O. Grubor-Urosevic, O. Tschauner, S. M. Clark, and R. T. Downs, High Pressure Research **33**, 466 (2013).
- [82] E. D. Bauer, V. A. Sidorov, S. Bobev, D. J. Mixson, J. D. Thompson, J. L. Sarrao, and M. F. Hundley *High-pressure investigation of the heavy-fermion antiferromagnet  $U_3Ni_5Al_{19}$*  Phys. Rev. B **71**, 014419 (2005).
- [83] D. Haskel (May 1999) *FLUO: Correcting XANES for self-absorption in fluorescence data*. <<http://www.aps.anl.gov/xfd/people/haskel/fluo.html>>

- [84] B. Ravel and M. Newville *ATHENA, ARTEMIS, HEPHAESTUS: data analysis for X-ray absorption spectroscopy using IFEFFIT*, Journal of Synchrotron Radiation **12**, 537–541 (2005).
- [85] P. Dera, B. Lavina, L. A. Borkowski, V. B. Prakapenka, S. R. Sutton, M. L. Rivers, R. T. Downs, N. Z. Boctor, and C. T. Prewitt, Geophys. Res. Lett. **35**, L10301 (2008).
- [86] J.P. Rueff *et al.*, Phys. Rev. Lett. **106** 186405 (2011).
- [87] J. L. Smith and E. A. Kmetko, J. Less. Common Metals **90**, 83 (1983).

## Curriculum Vitae

Daniel Antonio  
University of Nevada, Las Vegas  
Department of Physics and Astronomy  
4505 S. Maryland Pkwy  
Las Vegas, NV 89154  
(702) 895-2674  
antonio@physics.unlv.edu

### Education

University of Nevada, Las Vegas  
B.S., Physics, December 2004  
M.S., Physics, May 2009

### Publications

**High pressure effects on U  $L_3$  x-ray absorption near edge structure (XANES) and single crystal x-ray diffraction in heavy fermion compound  $UCd_{11}$**  Farzana Nasreen · [Daniel Antonio](#) · Derrick VanGennep · Andrew Cornelius · Corwin H. Booth Eric Bauer · Karunakar Kothapalli · Barbara Lavina · Curtis Kenney-Benson · Stanislav Sinogeikin · Changyong Park, *Journal of Physics: Condensed Matter*, submitted

**The Hardest Superconducting Metal Nitride** Shanmin Wang · [Daniel Antonio](#) · Xiaohui Yu · Jianzhong Zhang · Andrew L Cornelius · Duanwei He · Yusheng Zhao, *Scientific Reports* 09/2015; 5:13733

**High pressure transport and structural studies on  $Nb_3Ga$  superconductor** Vahe Mkrtchyan · Ravhi Kumar · Jason Baker · Anthony Connolly · [Daniel Antonio](#) · Andrew Cornelius · Yusheng Zhao, *Physica B Condensed Matter* 01/2015; 459.

**Effect of Pressure and Temperature on Structural Stability of  $MoS_2$**  Nirup Bandaru · Ravhi S. Kumar · Daniel Sneed · Oliver Tschauer · Jason Baker · [Daniel Antonio](#) · Sheng-Nian Luo · Thomas Hartmann · Yusheng Zhao · Rama Venkat, *The Journal of Physical Chemistry C* 02/2014; 118(6):3230–3235.

**ChemInform Abstract: Technetium Tetrachloride Revisited: A Precursor to Lower-Valent Binary Technetium Chlorides.** Erik V Johnstone · Frederic Poineau · Paul M Forster · Longzou Ma · Thomas Hartmann · Andrew Cornelius · [Daniel Antonio](#) · Alfred P Sattelberger · Kenneth R Czerwinski, *Inorganic Chemistry* 07/2012; 51(15):8462-7.

**Pressure effect on crystal structure and superconductivity of  $La_{0.8}Th_{0.2}FeAsO$**  Ravhi S. Kumar · [Daniel Antonio](#) · M. Kanagaraj · S. Arumugam · Andrew L. Cornelius · Stanislav Sinogeikin · J. Prakash · Gohil S. Thakur · A. K. Ganguli · T. Hartmann and Y. Zhao, *physica status solidi (RRL) - Rapid Research Letters* 06/2011; 5(5-6).

**Pressure induced structural transition and enhancement of superconductivity in Co doped CeFeAsO** Ravhi S. Kumar · Daniel Antonio · M. Kanagaraj · S. Arumugam · J. Prakash · Stanislav Sinogeikin · Gohil S. Thakur · A. K. Ganguli · Andrew Cornelius · Yusheng Zhao, *Applied Physics Letters* 01/2011; 98(1):012511-012511-3.

**Polarized inelastic neutron scattering of the partially ordered Tb<sub>2</sub>Sn<sub>2</sub>O<sub>7</sub>** K. C. Rule · G. Ehlers · J. R. Stewart · A. L. Cornelius · P. P. Deen · Y. Qiu · C. R. Wiebe · J. A. Janik · H. D. Zhou · D. Antonio · B. W. Woytko · J. P. Ruff · H. A. Dabkowska · B. D. Gaulin · J. S. Gardner, *Physical Review B* 12/2007; 76(21).

**Dynamics of diluted Ho spin ice Ho<sub>2-x</sub>Y<sub>x</sub>Ti<sub>2</sub>O<sub>7</sub> studied by neutron spin echo spectroscopy and ac susceptibility** G. Ehlers · J. S. Gardner · C. H. Booth · M. Daniel · K. C. Kam · A. K. Cheetham · D. Antonio · H. E. Brooks · A. L. Cornelius · S. T. Bramwell · J. Lago · W. Häussler · N. Rosov, *Physical review. B, Condensed matter* 04/2006; 73(17):174429.

**Antiferromagnetism in Pr<sub>3</sub>In** AD Christianson · J. M. Lawrence · J. L. Zarestky · H. S. Suzuki · J. D. Thompson · M. F. Hundley · J. L. Sarrao · C. H. Booth · D. Antonio · AL Cornelius, *Physical Review B* 07/2005; 72(2).